

Citation:

**Bucha B**, Sansò F (2021) Gravitational field modelling near irregularly shaped bodies using spherical harmonics: a case study for the asteroid (101955) Bennu, *Journal of Geodesy*, DOI: 10.1007/s00190-021-01493-w

Note: This is a preprint (author's own manuscript that has not been peer reviewed) of an article accepted for publication in *Journal of Geodesy*. The final authenticated version is available online at <https://doi.org/10.1007/s00190-021-01493-w>.

# Gravitational field modelling near irregularly-shaped bodies using spherical harmonics: a case study for the asteroid (101955) Bennu

Blažej Bucha · Fernando Sansò

Received: / Accepted:

**Abstract** We apply three spherical-harmonic-based techniques to deliver external gravitational field models of the asteroid (101955) Bennu within its circumscribing sphere. This region is known to be peculiar for external spherical harmonic expansions, because it may lead to a divergent series. The studied approaches are (i) spectral gravity forward modelling via external spherical harmonics, (ii) the least-squares estimation from surface gravitational data using external spherical harmonics, and (iii) the combination of internal and external series expansions. While the first method diverges beyond any reasonable doubts, we show that the other two methods may ensure relative accuracy from  $\sim 10^{-6}$  to  $10^{-8}$  in the vicinity of Bennu. This is possible even with the second method, despite the fact that it relies on a single series of external spherical harmonics. Our main motivation was to study conceptual differences between spherical harmonic coefficients from satellite data (analogy to the first method) and from surface gravitational data (the second method). Such coefficients are available through the popular spherical-harmonic-based models of the Earth's gravitational field and often are combined together. We show that the coefficients from terrestrial data may lead to a divergence effect of partial sums, though excellent accuracy can be achieved when such model is used in full. Under (presently) extreme but realistic conditions, the coefficients inconsistency may affect many near-surface geoscientific applications, such as the geoid/quasigeoid computation or residual terrain modelling. Computer codes (Fortran, MAT-

LAB) and data produced within the study are made freely available at <http://edisk.cvt.stuba.sk/~xbuchab/>.

**Keywords** Convergence/divergence of spherical harmonics · Gravity field modelling · Newton's integral · Spherical harmonics · Runge–Krup theorem

## 1 Introduction

On the global scale, the Earth's external gravitational field is often modelled by a finite linear combination of external spherical harmonics (e.g., Heiskanen and Moritz, 1967; Sansò and Sideris, 2013). One of the powerful features of spherical harmonics is the ability of spectral decomposition of the global gravitational field (e.g., Freedman and Schreiner, 2009; Jekeli, 2017). Spherical harmonics are advantageous also from the numerical viewpoint, as they offer efficient algorithms for gravity field modelling (e.g., Colombo, 1981; Sneeuw, 1994; Jekeli et al, 2007; Gruber et al, 2011; Balmino et al, 2012; Fukushima, 2012).

However, spherical harmonics are also subject to some limitations. For this study, the key drawback is that an infinite external spherical harmonic series of external gravitational potential may not necessarily converge on/below the smallest sphere encompassing the gravitating body, here called the sphere of convergence (Hotine, 1969). Somewhat paradoxically, such series related to the Earth's gravitational field are often evaluated on the Earth's surface, which, by definition, is always on/below this sphere. Examples from geodesy are the geoid/quasigeoid determination (e.g., Sjöberg, 2005; Wang et al, 2012), computation of Bouguer anomalies (e.g., Featherstone et al, 2013; Balmino et al, 2012), vertical datum unification (e.g., Grombein et al, 2017; Sansò et al, 2019) or residual terrain modelling (RTM; e.g., Forsberg and Tscherning, 1981; Hirt et al, 2019). Fortunately, the possible series divergence on the Earth's surface

---

Blažej Bucha

Department of Theoretical Geodesy, Slovak University of Technology in Bratislava, Radlinského 11, 81005 Bratislava, Slovak Republic  
E-mail: [blazej.bucha@stuba.sk](mailto:blazej.bucha@stuba.sk)

Fernando Sansò

Department of Civil and Environmental Engineering, Politecnico di Milano, Piazza Leonardo da Vinci 32, 20133 Milan, Italy  
E-mail: [fernando.sanso@polimi.it](mailto:fernando.sanso@polimi.it)

does not appear to be an issue in relation to current state-of-the-art models such as EGM2008 (Pavlis et al, 2012) or EIGEN-6C4 (Förste et al, 2014). Nevertheless, this may simply be because their accuracies and maximum harmonic degrees are still too low to reliably detect this effect. Once we move to simulation yet realistic numerical studies, it becomes clear that the series most likely diverges at least over some portions of the body's surface (e.g., Hu and Jekeli, 2015; Hirt et al, 2016; Hirt and Kuhn, 2017; Rexer, 2017; Šprlák et al, 2018; Bucha et al, 2019b).

More specifically, the limited global terrestrial gravity data coverage does not currently permit recovery of harmonics beyond degree  $\sim 720$  (spatial resolution of  $0.25^\circ$ ) solely from gravity measurements (e.g., Pavlis et al, 2012; Fecher et al, 2017; Pail et al, 2018). But since many applications require significantly higher spatial resolutions, the models are often supplemented by short-scale topography-derived gravity. This may require ultra-high-degree spherical harmonic modelling (e.g., Hirt et al, 2019), which, as it turns out, may produce divergent series on the Earth's surface (e.g., Hirt et al, 2016; Rexer, 2017; Bucha et al, 2019b). As a result, such combination may be theoretically invalid in the vicinity of the Earth's surface. The topography-implied gravitational field therefore nowadays reveals conditions that might be observed in the future, once the terrestrial gravity data coverage will enable to significantly exceed harmonic degree  $\sim 720$ .

It appears to be reasonable to expect that the accuracy and resolution of Earth's spherical-harmonic-based gravitational field models will follow the trend of continuous improvement that could be seen over the last few decades. Therefore, sooner or later, the series divergence on the Earth's surface may become a significant limitation for many day-to-day applications of these models. In fact, these limitations have already begun to emerge (e.g., Hirt et al, 2016; Rexer, 2017; Bucha et al, 2019b), necessitating further studies on the topic.

In this paper, we therefore numerically examine properties of three spherical-harmonic-based techniques. Having in mind near-surface applications such as that from the second paragraph, the region of key importance for our study is the domain below the sphere of convergence but outside the body. The studied techniques are

1. spectral gravity forward modelling (e.g., Martinec and Pěč, 1989; Rummel et al, 1988; Wiczorek and Phillips, 1998; Balmino et al, 2012; Hirt and Kuhn, 2014; Wiczorek, 2015),
2. the least-squares estimation from surface gravitational data using a fully-occupied normal equations matrix (e.g., Sansò, 1982; Pavlis, 1988; Sacerdote and Sansò, 2010; Fecher et al, 2017), and
3. the combination of internal and external series expansions (e.g., Sjöberg, 1977; Jekeli, 1983; Grafarend and Engels, 1993; Wang, 1997; Martinec, 1998).

The first approach represents external gravitational field modelling via external spherical harmonic series. Such series is studied in many classical textbooks on potential theory (e.g., Hobson, 1931; Heiskanen and Moritz, 1967; Hotine, 1969; Martinec, 1998; Freedman and Schreiner, 2009) and can be estimated in practice, for instance, from satellite gravitational data. Due to its convergence issues within our target region, we focus on the second method. It also leads to an external spherical harmonic series, but is expected to be able to reproduce surface gravitational data with an arbitrary  $\varepsilon$ -accuracy,  $\varepsilon > 0$ . Key for this study is, however, that the output series differs conceptually from the first method (Sansò and Sideris, 2013; Sacerdote and Sansò, 2010). In practice, these models can be estimated, for instance, from surface gravitational data. The third method is yet another approach suitable to gravitational field modelling below the sphere of convergence. Unlike the two previous methods, it combines internal and external series expansions, which depend on the radius of the evaluation point.

Our studied gravitational field is generated by the asteroid (101955) Bennu (Fig. 1). We opted for this asteroid, because its irregular shape causes series divergence near its surface at degrees as low as a few tens (Sebera et al, 2016), thereby significantly reduces computational costs of the study in the range of critical frequencies. For a comparison, the series divergence on the Earth's surface was reported to emerge at degree  $\sim 10,800$  (e.g., Hirt et al, 2016; Rexer, 2017; Bucha et al, 2019b). To allow for accurate gravitational field modelling, we derive a smooth analytical shape of Bennu based on Fig. 1. After assuming a constant-mass density, we obtain a mathematically well-defined, realistic yet sufficiently simple model of Bennu that generates a complex gravitational field.

When combining the carefully designed closed-loop environment and high-performance computing facilities, this allows us to scrutinize the three techniques to high accuracy levels. Hopefully, this might reveal some behaviour that could not be seen previously due to the data noise and/or because of insufficient resolutions of gravity field models. Such experiments might lead to a better understanding of modern spherical-harmonic-based Earth's gravitational field models, which are still associated with some open issues (e.g., Sansò and Sideris, 2013; Sacerdote and Sansò, 2010; Bucha et al, 2019c). Some of these topics will be addressed in this paper.

The outline of the paper is as follows. After describing the gravitating body in Section 2, we discuss the three studied spherical-harmonic-based methods in Section 3. These techniques are then applied in numerical experiments in Sec-

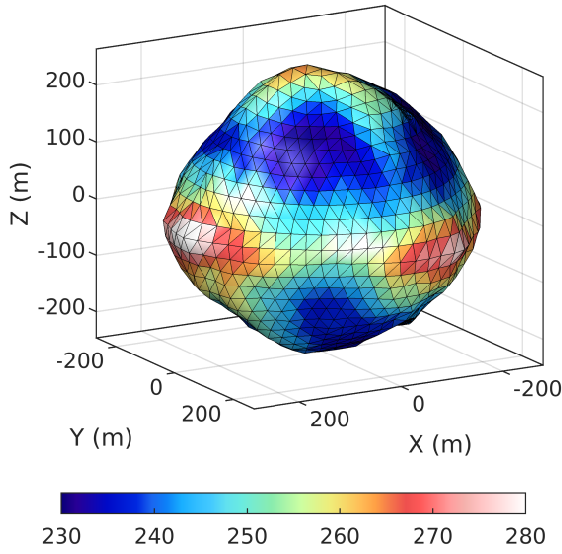


**Fig. 1** (101955) Benu as provided by the EAR-A-I0037-5-BENNUSHAPE-V1.0 shape model (Nolan et al, 2013). The resolution of the model is  $\sim 25$  m. Colour bar in metres

tion 4, after which we provide a discussion in Section 5. Finally, conclusions are drawn in Section 6.

## 2 Gravitating body

We approximate Benu by a band-limited shape model and a constant mass density distribution. Here, the Benu's shape  $S$  is expanded into a truncated surface spherical harmonic series (see Fig. 2),

$$r_S(\varphi, \lambda) = \sum_{n=0}^{N_S} \sum_{m=-n}^n \bar{r}_{nm}^S \bar{Y}_{nm}(\varphi, \lambda), \quad (1)$$

where  $r_S$  is the spherical radius of a surface point with the spherical latitude  $\varphi$  and the longitude  $\lambda$ ,  $\bar{Y}_{nm}$  are the  $4\pi$ -fully-normalized surface spherical harmonics of degree  $n$  and order  $m$  (e.g., Heiskanen and Moritz, 1967),  $\bar{r}_{nm}^S$  are the spherical harmonic coefficients and  $N_S$  is the maximum degree of the expansion, here being equal to 15. The spectrum of the Benu's shape is shown in Fig. 3.

Our physical model of Benu is finally obtained after assigning a single-constant mass density of  $\rho = 1260 \text{ kg m}^{-3}$  (Chesley et al, 2014) to the degree-15 surface expansion from Fig. 2. The parameters of the Benu model are summarized in Table 1. Included are also radii of four spheres that are relevant for this study:

- the Bjerhammar sphere  $\underline{\Omega}$  with the radius  $0 < \underline{R} < \min(r_S)$  (a sphere completely below the body's surface),
- the mean sphere  $\Omega$  with the radius  $R = \bar{r}_{00}^S$  (a sphere partially cutting the body),
- the sphere of convergence  $\Omega_c$  with the radius  $R_c = \max(r_S)$  (a sphere just touching the body), and

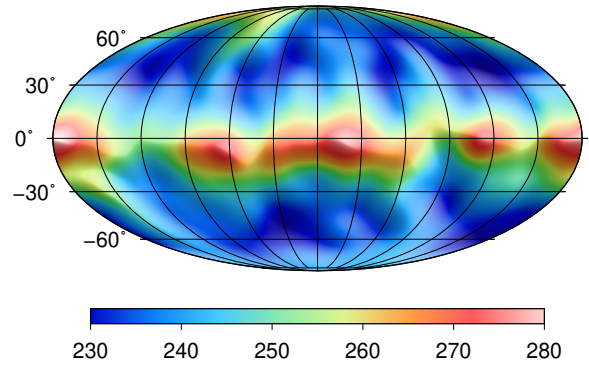


**Fig. 2** Surface spherical harmonic expansion of the Benu's shape  $S$  in terms of the spherical radius  $r_S$  (m) synthesized up to degree  $N_S = 15$  using Eq. (1). This shape and a constant mass density of  $\rho = 1260 \text{ kg m}^{-3}$  represent the physical model of Benu, the gravitational field of which is studied in this paper. The  $\bar{r}_{nm}^S$  coefficients from Eq. (1) were computed from the polyhedral model depicted in Fig. 1 by harmonically analysing a grid of the Benu's radii  $r_S$  via the Gauss–Legendre quadrature (e.g., Sneeuw, 1994). Since the quadrature points are different from those in the polyhedral model, we computed  $r_S$  at each quadrature point before applying the harmonic analysis. This was accomplished by finding intersections of rays from the origin of the coordinate system determined by the latitudes and longitudes (given by the quadrature) with the polyhedral model. Then, the harmonic analysis was performed up to degree 1000 to mitigate the aliasing. In this study, only the coefficients up to degree 15 are used (Fig. 3). The map is centred at the meridian  $180^\circ$ .

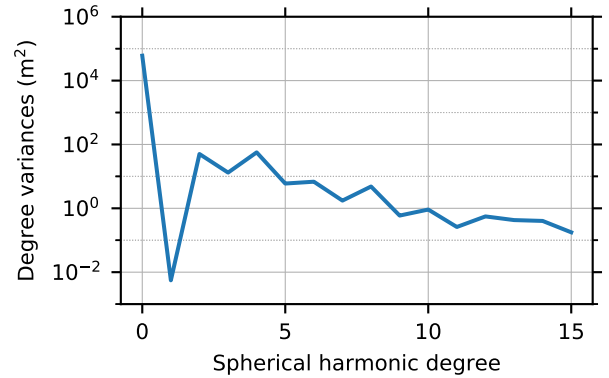


**Fig. 3** Spectrum of the Benu's shape as represented by surface spherical harmonic expansion up to degree  $N_S = 15$  via Eq. (1)

- the Brillouin sphere  $\bar{\Omega}$  with the radius  $\bar{R} > \max(r_S)$  (a sphere completely outside the body).

The radii  $\underline{R}$  and  $\bar{R}$  were found by rounding  $\min(r_S)$  and  $\max(r_S)$  to the nearest integers that are smaller and larger than these values, respectively.

In the paper, we often use the term *irregular* in relation to a body's shape. Here, the irregularity is measured simply by the ratio between the radii of the sphere of convergence and of the largest Bjerhammar sphere. We call this parameter the shape ratio. As a rule of thumb, the larger the shape ratio, the more difficult it is to accurately model surface gravitational fields via external spherical harmonics.

**Table 1** Geometrical and physical parameters defining the model of Bennu and some other parameters used throughout the study

Density $\rho$	$1260 \text{ kg m}^{-3}$
Shape $S$	$\tilde{r}_{nm}^S$ up to degree $n_{\max} = 15$
Radius $\underline{R}$ of the Bjerhammar sphere $\underline{\Omega}$	224 m
Radius $R$ of the mean sphere $\Omega$	$\approx 245.284 \text{ m}$
Radius $R_c$ of the sphere of convergence $\Omega_c$	$\approx 282.5 \text{ m}$
Radius $\bar{R}$ of the Brillouin sphere $\bar{\Omega}$	283 m
Newton's gravitational constant $G$	$6.67384 \times 10^{-11} \text{ m}^3 \text{ kg}^{-1} \text{ s}^{-2}$

As an illustration, the Bennu's shape ratio roughly equals to  $282.5 \text{ m}/224 \text{ m} \approx 1.261$  (see Table 1), while for the Earth, it reads only  $6384.403 \text{ km}/6356.752 \text{ km} \approx 1.004$ .<sup>1</sup> The series divergence for Bennu will therefore likely to emerge at much lower harmonic degrees than for the Earth (see Introduction).

In this study, the input shape and density models are considered as errorless. This allows to perform closed-loop experiments with almost an arbitrary accuracy, so that the studied techniques can be examined thoroughly. For instance, our reference surface gravitational data are accurate up to the 14th digit in double precision. Obviously, imperfections of the shape and density model (measurement errors in the original shape model, limited resolution, etc.) make this accuracy level useless in relation to the true gravitational field of Bennu. Nevertheless, the accuracy is crucial for the closed-loop tests.

We acknowledge that there exist more recent polyhedral models of the Bennu's shape derived from the OSIRIS-REx mission reaching resolutions up to  $\sim 0.8 \text{ m}$  (e.g., Barnouin et al, 2019). Given the closed-loop nature of our experiments and the rather low-degree surface expansion of our shape model (Fig. 2), we find the polyhedral model by Nolan et al (2013) from Fig. 1 to be sufficient for this study.

### 3 Methods

In this section, we briefly recapitulate the three studied spherical-harmonic-based approaches for gravitational field modelling: spectral gravity forward modelling (Section 3.1), the least-squares estimation from surface gravitational data (Section 3.2), and the combination of internal and external series expansions (Section 3.3). For each method, we discuss its applications and highlight some open topics to be studied numerically in Section 4.

Importantly, each method, in one way or another, necessarily relies on a regularization, for instance, by truncating infinite spherical harmonic series or by using a computer number format of finite precision (e.g., double or quadruple precision). Therefore, all the names of methods we use must be accompanied by the adjective *regularized*. However, to

avoid the somewhat cumbersome language, we omit the adjective. Nevertheless, it is to be understood throughout the paper that all our modelling techniques and subsequently all the models are regularized, which is a property that can only rarely be avoided in practice, but is of key importance for understanding the underlying concepts.

#### 3.1 Spectral gravity forward modelling

This technique delivers a solid external spherical harmonic expansion of an external gravitational potential implied by a body having its shape expanded into surface spherical harmonics (cf. Eq. 1). In this paper, we additionally assume a constant mass density  $\rho$ . The method is relevant for this study, because this type of expansion (i) is the one that is commonly discussed in many textbooks on gravitational field modelling (e.g., Hobson, 1931; Heiskanen and Moritz, 1967; Hotine, 1969; Martinec, 1998; Freedden and Schreiner, 2009) and (ii) can be estimated in practice from satellite gravitational measurements (Sacerdote and Sansò, 2010; Sansò and Sideris, 2013).

In this method, we split the Bennu's gravitational potential into two constituents,

$$V^{\text{SGFM}}(r, \varphi, \lambda) = V_{\text{ball}}(r) + V_{\text{res}}^{\text{SGFM}}(r, \varphi, \lambda), \quad (2)$$

where  $V_{\text{ball}}(r)$  is the gravitational field of the homogeneous ball with the radius  $\underline{R}$  (the Bjerhammar sphere from Table 1) and  $V_{\text{res}}^{\text{SGFM}}(r, \varphi, \lambda)$  is the gravitational potential implied by the masses residual to the ball. Both  $V_{\text{ball}}$  and  $V_{\text{res}}^{\text{SGFM}}$  rely on the same constant mass density  $\rho$ . Finally,  $(r, \varphi, \lambda)$  are the spherical radius, the spherical latitude and the longitude of the evaluation point, respectively.

The first term on the right-hand side of Eq. (2) is given by the simple relation,

$$V_{\text{ball}}(r) = \frac{GM_{\text{ball}}(\underline{R})}{r}, \quad (3)$$

where  $G$  is Newton's gravitational constant and

$$M_{\text{ball}}(\underline{R}) = \frac{4}{3} \rho \pi \underline{R}^3 \quad (4)$$

is the mass of the ball.

<sup>1</sup> For the Earth, the first radius is taken from Sjöberg (1977) and the other one equals to the semi-minor axis of GRS80 (Moritz, 2000).

To obtain the other term,  $V_{\text{res}}^{\text{SGFM}}(r, \varphi, \lambda)$ , we introduce at first topographic heights  $\hat{H}(\varphi, \lambda)$  measured in spherical approximation from the Bjerhammar sphere  $\underline{\Omega}$ ,

$$\hat{H}(\varphi, \lambda) = r_S(\varphi, \lambda) - \underline{R}, \quad (5)$$

and a dimensionless topographic height function,

$$H(\varphi, \lambda) = \frac{\hat{H}(\varphi, \lambda)}{\underline{R}}. \quad (6)$$

Spherical harmonic coefficients of  $H(\varphi, \lambda)$  therefore read

$$\bar{H}_{nm} = \begin{cases} \frac{\bar{r}_{00}^S - \underline{R}}{\underline{R}} & \text{for } n = 0, m = 0, \\ \frac{\bar{r}_{nm}^S}{\underline{R}} & \text{otherwise.} \end{cases} \quad (7)$$

Note that  $\hat{H}(\varphi, \lambda)$  and  $H(\varphi, \lambda)$  are always positive and both are band-limited up to degree  $N_S$  (see Eq. 1).

Then, for evaluation points with  $r > \max(r_S)$ , spectral gravity forward modelling yields truncated solid spherical harmonic expansion (e.g., Martinec, 1998),

$$V_{\text{res}}^{\text{SGFM}}(r, \varphi, \lambda) = \frac{GM}{\bar{R}} \sum_{n=0}^{N_{\text{SGFM}}} \left( \frac{\bar{R}}{r} \right)^{n+1} \times \sum_{m=-n}^n \bar{V}_{nm}^{\text{SGFM}} \bar{Y}_{nm}(\varphi, \lambda), \quad (8)$$

where  $\bar{V}_{nm}^{\text{SGFM}}$  are the spherical harmonic coefficients of  $V_{\text{res}}^{\text{SGFM}}$  given as

$$\bar{V}_{nm}^{\text{SGFM}} = \frac{4\pi\rho\bar{R}^3}{(2n+1)M} \left( \frac{\bar{R}}{\bar{R}} \right)^n \sum_{p=1}^{p_{\max}} \frac{1}{p} \binom{n+2}{p-1} \bar{H}_{nmp}, \quad (9)$$

with  $\bar{H}_{nmp}$  being spherical harmonic coefficients of  $H^p(\varphi, \lambda)$  that are generally non-zero up to degree  $p \times N_S$  (e.g., Hirt and Kuhn, 2014; Bucha et al, 2019a). In the two equations,  $M$  is the mass of Bennu. Although unnecessary, because it appears in the numerator (Eq. 8) and denominator (Eq. 9), it was introduced for conventional reasons. The particular value of  $M$  can therefore be any non-zero real number. Throughout the paper, we use  $M = 7.8 \times 10^{10}$  kg (Chesley et al, 2014). Finally, the series over  $n$  and  $p$  are infinite in theory, but have to be truncated in practice.

In Eq. (9), we introduced the  $(\bar{R}/\bar{R})^n$  term to rescale  $\bar{V}_{nm}^{\text{SGFM}}$  from the Bjerhammar sphere  $\underline{\Omega}$  to the Brillouin sphere  $\bar{\Omega}$  (upward continuation in the spectral domain). We therefore say that the  $\bar{V}_{nm}^{\text{SGFM}}$  coefficients in Eq. (8) refer to the Brillouin sphere with the radius  $\bar{R}$ . Importantly, such rescaling does not affect the behaviour of the truncated series (8) and (9), because after substituting Eq. (9) into (8),  $\bar{R}$  vanishes for any  $\bar{R} \neq 0$ . Nevertheless, we opted for the rescaling procedure, mainly for theoretical reasons described in Theorem 4 of Sansò and Sideris (2013).

For this paper, the key property of Eq. (8) is that, even if we push  $N_{\text{SGFM}}$  to infinity, it uniformly converges above the sphere of convergence with the radius  $R_c = \max(r_S(\varphi, \lambda))$ , but on/below this sphere, it may converge or diverge (e.g., Balmino, 1994). Generally, this opens some questions, the following three of which are sometimes discussed in the literature.

1. For the real Earth, this type of expansion is sometimes considered to be an asymptotic series<sup>2</sup> (e.g., Moritz, 2003; Sjöberg and Bagherbandi, 2017).
2. In other places, a conclusion can be found that since the expansion is always finite in practice, the convergence is not a problem (e.g., Sjöberg and Bagherbandi, 2011; Sjöberg, 2015).
3. Martinec (1998) acknowledges on Page 86 that (using our notation)

*[...] since  $|\bar{V}_{nm}^{\text{SGFM}}| < \infty$ , the finite series (8) has finite values not only outside the bounding sphere  $r = R_c$ , but also in the space between the Earth's surface and the sphere  $r = R_c$ . Therefore,  $V_{\text{res}}^{\text{SGFM}}$  represented by the finite series (8) can be considered as the reference gravitational potential for gravity observations performed on the Earth's surface.*

These topics will be studied numerically in Section 4.

### 3.2 Least-squares estimation from gravitational surface data

Similarly as spectral gravity forward modelling, this technique approximates external gravitational field through a single set of external spherical harmonics. The conceptual difference, however, is that it approximates, up to some specified  $\varepsilon$ -accuracy,  $\varepsilon > 0$ , the gravitational field also below the sphere of convergence (but outside the masses), where the previous technique may diverge (Sacerdote and Sansò, 2010; Sansò and Sideris, 2013). The existence of such solution is supported by the Runge–Krarup theorem (Krarup, 1969; Moritz, 1980; Freedman, 1980; Sansò and Sideris, 2013; Augustin et al, 2018).<sup>3</sup> Usually, these models come into play whenever the resolution of satellite-based models needs to be enhanced by surface gravity data. Their development is, however, not trivial, for instance, because data residing on the body's surface lead to a fully-populated

<sup>2</sup> Gradshteyn and Ryzhik (2007) acknowledge on asymptotic series that (Page 21) *despite the fact that these series diverge, the values of the functions that they represent can be calculated with a high degree of accuracy if we take the sum of a suitable number of terms of such series.*

<sup>3</sup> In our case, the Bennu's surface  $S$  given by Eq. (1) is sufficiently regular. Therefore, one can refer to the Keldysh–Lavrentiev theorem (e.g., Moritz, 1980), implying that the  $\varepsilon$ -accuracy can theoretically be achieved not only above Bennu, but also on its surface.

normal equations matrix (e.g., Sansò and Sideris, 2013). Solving such a linear system of equations is currently computationally expensive if the maximum degree is, say, a few hundreds or higher. This technique has been used to develop the TUM2013C (Fecher et al, 2015), GOCO05c (Fecher et al, 2017) and XGM2016 (Pail et al, 2018) models.

To estimate the spherical harmonic coefficients by the least-squares method, we set up at first a linear system of equations (e.g., Sacerdote and Sansò, 2010; Sansò and Sideris, 2013)

$$\frac{GM}{R} \sum_{n=0}^{N_{LS}} \sum_{m=-n}^n \bar{V}_{nm}^{LS} (\bar{S}_{nm}(r_S, \varphi, \lambda), \bar{S}_{jk}(r_S, \varphi, \lambda))_{L^2(\omega)} \quad (10)$$

$$= (V(r_S, \varphi, \lambda), \bar{S}_{jk}(r_S, \varphi, \lambda))_{L^2(\omega)}, \quad (r_S, \varphi, \lambda) \in S,$$

where  $V(r_S, \varphi, \lambda)$  is the surface gravitational potential,  $\bar{S}_{nm}(r_S, \varphi, \lambda)$  are solid spherical harmonics defined as

$$\bar{S}_{nm}(r_S, \varphi, \lambda) = \left(\frac{R}{r_S}\right)^{n+1} \bar{Y}_{nm}(\varphi, \lambda), \quad (11)$$

and, finally, the scalar products read (cf. Remark 3.1 of Sacerdote and Sansò, 2010)

$$(f, g)_{L^2(\omega)} = \frac{1}{4\pi} \iint_{\omega} f(\varphi, \lambda) g(\varphi, \lambda) d\omega(\varphi, \lambda), \quad (12)$$

with  $\omega$  being the unit sphere. Note that  $r_S(\varphi, \lambda)$  in Eq. (10) is variable and, in our study, is defined by Eq. (1). Numerical aspects of Eq. (10) will be discussed in Section 4.3.

Solving the linear system (10) using the least-squares method yields the sought spherical harmonic coefficients, which we denote as  $\bar{V}_{nm}^{LS}(N_{LS})$ . These are related to the gravitational potential as

$$V^{LS}(r, \varphi, \lambda) = \frac{GM}{R} \sum_{n=0}^{N_{LS}} \left(\frac{R}{r}\right)^{n+1} \sum_{m=-n}^n \bar{V}_{nm}^{LS}(N_{LS}) \bar{Y}_{nm}(\varphi, \lambda). \quad (13)$$

Noteworthy, while  $\bar{V}_{nm}^{SGFM}$  from Eq. (8) refer to the Brilouin sphere  $\bar{\Omega}$ ,  $\bar{V}_{nm}^{LS}(N_{LS})$  refer to the Bjerhammar sphere  $\underline{\Omega}$  (note the radius of the Bjerhammar sphere  $\underline{R}$  in Eq. 13). The two sets of coefficients therefore have to be rescaled to a common sphere before they can be mutually compared (e.g., Barthelmes, 2013).

As already mentioned, Eq. (13) is able to approximate the external gravitational potential on and above our model of Bennu with an arbitrary  $\varepsilon$ -accuracy,  $\varepsilon > 0$ , as opposed to Eq. (8), which may be valid only above the sphere of convergence  $\Omega_c$ . Another difference is that the  $\bar{V}_{nm}^{LS}(N_{LS})$  coefficients depend on the maximum degree of the expansion  $N_{LS}$  (e.g., Freedman, 1980; Sansò, 1982; Sacerdote and Sansò, 2010; Sansò and Sideris, 2013; Augustin et al, 2018), while the  $\bar{V}_{nm}^{SGFM}$  coefficients from Eq. (8) are independent of

$N_{SGFM}$ . Furthermore, according to Sansò and Sideris (2013) (see also Sacerdote and Sansò, 2010), it holds that

$$\lim_{N_{LS} \rightarrow \infty} \bar{V}_{nm}^{LS}(N_{LS}) = \bar{V}_{nm}^{SGFM}. \quad (14)$$

However, as mentioned by Sansò and Sideris (2013), the limit

$$\lim_{N_{LS} \rightarrow \infty} \frac{GM}{R} \sum_{n=0}^{N_{LS}} \left(\frac{R}{r}\right)^{n+1} \sum_{m=-n}^n \bar{V}_{nm}^{LS}(N_{LS}) \bar{Y}_{nm}(\varphi, \lambda) \quad (15)$$

does *not* exist in general at points on  $S$ .

From our literature overview, we could not find any previous numerical studies that would compare the least-squares solution from Eq. (13) with the type of the harmonic series from Eq. (8), nor we were able to find a numerical demonstration of Eq. (14). In Section 4, we therefore conduct such experiments in a complex yet accurate closed-loop environment, revealing numerically the conceptual differences between the two equations (see, e.g., Sacerdote and Sansò, 2010).

### 3.3 Combination of internal and external series expansions

This method is fundamentally different from the two previous techniques. The previous methods always approximate the external (harmonic) gravitational potential at points external to the body and its (*regularized*) analytical downward continuation inside the body. The combination of internal and external series expansions, on the other hand, describes the external (harmonic) potential whenever the computation point is external to the body and the internal (non-harmonic) potential at points inside the body. That is, the method is valid everywhere in the space, including the body's surface and the space below it. Contrary to Section 3.2, it does not rely on the Runge–Krarup theorem. The combination of internal and external series expansions can be used, for instance, to determine the geoid (e.g., Martinec, 1998), which is partially inside the masses, or for gravity field modelling on the body's surface (e.g., Górski et al, 2018).

Typical for this method is that if the spherical radius of the computation point  $r$  satisfies the inequality  $r \leq \max(r_S)$ , then the spherical harmonic coefficients depend on  $r$ . Otherwise, one arrives at the traditional external spherical harmonic series that is convergent above  $\max(r_S)$ , such as that from Section 3.1. In this paper, we are mostly interested in gravitational field modelling within the problematic space between  $\min(r_S)$  and  $\max(r_S)$ . But since the coefficients then depend on  $r$ , we limit ourselves for simplicity only to the computation points on the mean sphere  $\Omega$  from Table 1, that is, with  $r = R$ . The mean sphere is partially outside and partially inside the masses, meaning that we deal now with harmonic and non-harmonic potentials, respectively.

We decompose the gravitational potential of Bennu on  $\Omega$  as follows,

$$\begin{aligned} V^{\text{IE}}(R, \varphi, \lambda) &= V_{\text{ball}}(R) + V^{\text{Ext}}(R, \varphi, \lambda) + V^{\text{Int}}(R, \varphi, \lambda) \\ &= V_{\text{ball}}(R) + V_{\text{res}}^{\text{IE}}(R, \varphi, \lambda). \end{aligned} \quad (16)$$

Here,  $V_{\text{ball}}$  is the gravitational potential due to the homogeneous ball with the radius  $R$  and the mass  $M_{\text{ball}}(R)$  (see Eq. 4), and is given by Eq. (3).  $V^{\text{Ext}}$  is the gravitational potential of the masses that are present inside the ball, but are actually outside Bennu. This value is therefore negative and the sum  $V_{\text{ball}} + V^{\text{Ext}}$  yields the gravitational potential of Bennu's masses below  $\Omega$ . Finally,  $V^{\text{Int}}$  represents the gravitational potential of the Bennu's masses above  $\Omega$ .

Here, the  $V^{\text{Ext}}$  term is modelled by a spherical harmonic series (e.g., Martinec, 1998),

$$V^{\text{Ext}}(R, \varphi, \lambda) = \frac{GM}{R} \sum_{n=0}^{N_{\text{Ext}}} \sum_{m=-n}^n \bar{V}_{nm}^{\text{Ext}}(R) \bar{Y}_{nm}(\varphi, \lambda) \quad (17)$$

with

$$\bar{V}_{nm}^{\text{Ext}}(R) = \frac{4\pi \rho R^3}{(2n+1)M} \sum_{p=1}^{p_{\text{max}}^{\text{Ext}}} \frac{1}{p} \binom{n+2}{p-1} \bar{H}_{nmp}^{(r_S \leq R)}, \quad (18)$$

and  $V^{\text{Int}}$  is expanded as (ibid.)

$$V^{\text{Int}}(R, \varphi, \lambda) = \frac{GM}{R} \sum_{n=0}^{N_{\text{Int}}} \sum_{m=-n}^n \bar{V}_{nm}^{\text{Int}}(R) \bar{Y}_{nm}(\varphi, \lambda) \quad (19)$$

with

$$\bar{V}_{nm}^{\text{Int}}(R) = \frac{4\pi \rho R^3}{(2n+1)M} \sum_{p=1}^{p_{\text{max}}^{\text{Int}}} \frac{1}{p} \binom{-n+1}{p-1} \bar{H}_{nmp}^{(r_S \geq R)}. \quad (20)$$

In Eqs. (18) and (20),  $\bar{H}_{nmp}^{(r_S \leq R)}$  and  $\bar{H}_{nmp}^{(r_S \geq R)}$  are surface spherical harmonic coefficients of the  $p$ th power of, respectively,

$$H^{(r_S \leq R)} = \begin{cases} 0 & \text{for } r_S > R, \\ \frac{r_S - R}{R} & \text{otherwise,} \end{cases} \quad (21)$$

and

$$H^{(r_S \geq R)} = \begin{cases} 0 & \text{for } r_S < R, \\ \frac{r_S - R}{R} & \text{otherwise.} \end{cases} \quad (22)$$

Due to the abrupt changes in the shape of  $H^{(r_S \leq R)}$  and  $H^{(r_S \geq R)}$ , their spectra are infinite, even though  $r_S$  is band-limited to degree  $N_S$  (see Eq. 1). In the numerical computations, the parameters  $N_{\text{Ext}}$  and  $N_{\text{Int}}$  should therefore be as large as reasonably possible. Note that only *surface* spherical harmonics are involved in Eqs. (17) and (19), and that the coefficients  $\bar{V}_{nm}^{\text{Int}}$  and  $\bar{V}_{nm}^{\text{Ext}}$  refer to the mean sphere  $\Omega$ .

In Section 4, we study the convergence speed of Eq. (16) as a function of  $N_{\text{Ext}} = N_{\text{Int}}$  and  $p_{\text{max}}^{\text{Ext}} = p_{\text{max}}^{\text{Int}}$  against accurate reference values. In addition, we investigate which of the two series, Eq. (13) or (16), offers the most rapid convergence over parts of the mean sphere  $\Omega$  that are in the mass-free space, in which both techniques can be applied.

## 4 Numerical experiments

### 4.1 Reference gravitational data – Spatial gravity forward modelling

Due to the lack of real gravitational data on the Bennu's surface and in its vicinity, we are forced to compute them by gravity forward modelling. To ensure independence from the studied spectral techniques, this should be done by spatial-domain divergence-free gravity forward modelling. To this end, we employed the method of Fukushima (2017) and computed three grids of the reference gravitational potential  $V^{\text{Ref}}$  that will be used as a benchmark (Table 2). As an example, the surface gravitational potential is shown in Fig. 4.

Briefly, the method of Fukushima (2017) relies on the double exponential rule. We took advantage of the `dqde.f90` Fortran subroutine (Fukushima, 2017), which computes a line integral<sup>4</sup>

$$\int_a^b f(x) dx \quad (23)$$

with some relative error tolerance  $\delta$ . After specifying the  $\delta$  parameter, the algorithm automatically takes care of the evaluation of the integrand at suitable points  $x$  and stops when the desired accuracy is met. Because of this, the sampling points are generally not known prior to the integration and, therefore, it is difficult to prepare a suitable grid of  $f(x)$  beforehand. This is certainly true when considering that the sampling points vary not only with  $\delta$ , but also from integrand to integrand. In our case, this means that each evaluation point  $(r, \varphi, \lambda)$  likely requires its own sampling points  $(\varphi', \lambda')$ . For this reason and to narrow numerical errors, we compute the sampling values of  $f(x)$  rigorously on-the-fly, avoiding any interpolation. This means to evaluate  $r_S(\varphi', \lambda')$  from Eq. (1) repeatedly at various  $(\varphi', \lambda')$  until the specified accuracy  $\delta$  is reached at the particular evaluation point  $(r, \varphi, \lambda)$ . From the `dqde.f90` subroutine, we developed a Fortran and MATLAB package tailored to our needs. The package is named GFM.DE.rule (gravity forward modelling using the double exponential rule) and is freely available for download at <http://edisk.cvt.stuba.sk/~xbuchab/>.

<sup>4</sup> The integral can be weakly singular.



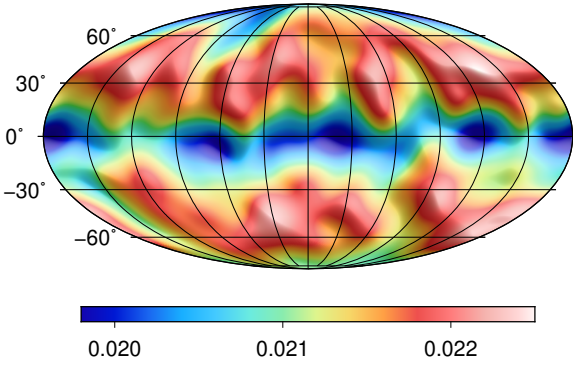


**Fig. 4** Reference gravitational potential on the Benu's surface in  $\text{m}^2 \text{s}^{-2}$ . The spatial distribution of the dataset is specified in the caption of Table 2. The table also lists some statistics of the data (the first row). The map is centred at the meridian  $180^\circ$

Although this approach may lead to long computation times, it allows us to achieve any accuracy we need essentially. For the reference gravitational potential  $V^{\text{Ref}}$ , we decided to use  $\delta = 10^{-16}$  in double precision. Based on an independent validation on the Brillouin sphere with respect to spectral gravity forward modelling (see Fig. 7 in Section 4.2), we expect the reference data to be accurate up to the 14th digit at  $\sim 99\%$  of the points. Due to its accuracy, flexibility and efficiency, the method of Fukushima (2017) is one of the key prerequisites that enable us to achieve high accuracy levels within our closed-loop environment.

#### 4.2 Spectral gravity forward modelling

Using Eq. (9), we computed the  $\bar{V}_{nm}^{\text{SGFM}}$  coefficients up to degree  $N_{\text{SGFM}} = 225$ , while using  $p_{\text{max}} = 228$  powers of  $H^p(\varphi, \lambda)$ . Importantly, the obtained coefficients do *not* suffer from errors due to the truncation of the binomial series (9), because  $H^p(\varphi, \lambda)$  with  $p > 228$  no longer contribute to  $\bar{V}_{nm}^{\text{SGFM}}$  within the studied bandwidth. This follows from the same equation, which tells us that the gravitational contribution of  $\bar{H}_{nmp}$  to  $\bar{V}_{nm}^{\text{SGFM}}$  may be non-zero only for harmonic degrees  $\max(0, p-3), \dots, p \times N_S$ , where  $N_S$  is the maximum degree from Eq. (1), here assumed to be a positive integer.

Other possible error sources in spectral gravity forward modelling are eliminated down to the computational precision. First, we use the Gauss–Legendre quadrature for spherical harmonic analysis (e.g., Sneeuw, 1994). This quadrature is exact provided that the input signal is band-limited, which holds true for our  $H^p(\varphi, \lambda)$  (see Section 3.1). Second, the aliasing in spherical harmonic analysis is mitigated by the proper sampling of  $H^p(\varphi, \lambda)$  after Hirt and Kuhn (2014) and Bucha et al (2019a). Third, the entire forward modelling process was conducted in quadruple precision in order to completely avoid the numerical issues discussed by

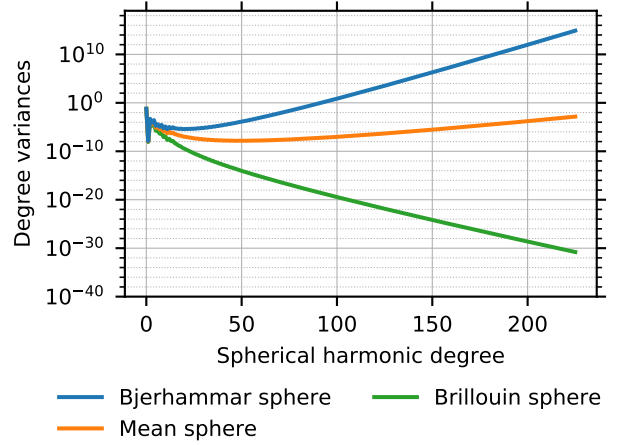


**Fig. 5** Spectrum of  $V_{\text{res}}^{\text{SGFM}}$  from Eq. (8) (dimensionless). The degree variances are referenced to three different spheres by properly rescaling the original spherical harmonic coefficients from the Brillouin sphere (see, e.g., Barthelmes, 2013)

Bucha et al (2019b) in their Section 4.2.2. After converting  $\bar{V}_{nm}^{\text{SGFM}}$  from quadruple to double precision, the final coefficients are obtained that will be used throughout the paper unless stated otherwise. As a conclusion, it can be said that the coefficients are computed *analytically*, avoiding any approximations besides that due to the limited computational precision.

In Fig. 5, we show the complete spectrum of  $V_{\text{res}}^{\text{SGFM}}$ . The gravitational contributions due to the individual powers  $H^p(\varphi, \lambda)$ ,  $p = 1, \dots, 228$ , are shown in Fig. 6. The former figure indicates a severe divergence effect on the Benu's surface already at degree  $\sim 25$ . However, the two diverging spectra refer to the mean sphere (partially inside the masses) and to the Bjerhammar sphere (completely below the Benu's surface) which may be misleading when interpreting an external gravitational field. To examine the series behaviour below the sphere of convergence, we therefore rely on a spatial-domain validation on the Benu's surface.

To analyse the results in the spatial domain, we use the following measure,

$$\delta V(r, \varphi, \lambda) = \left| \frac{V^{\text{SGFM}}(r, \varphi, \lambda) - V^{\text{Ref}}(r, \varphi, \lambda)}{V^{\text{Ref}}(r, \varphi, \lambda)} \right|, \quad (24)$$

where  $V^{\text{SGFM}}$  is given by Eq. (2) and  $V^{\text{Ref}}$  is the reference gravitational potential from Section 4.1. The outcomes of validations on the Brillouin sphere and on the Benu's surface are shown in Figs. 7 and 8, respectively. On the Brillouin sphere (Fig. 7), where the spectral technique converges by definition, excellent accuracy is achieved, reaching 14-digit agreement or better in the vast majority of points. However, the situation is radically different on the Benu's surface (Fig. 8), where the convergence is no longer guaranteed. Here, the accuracy significantly decreases, even to the 0-digit agreement for a large portion of the Benu's surface.



**Table 2** Statistics of the reference gravitational. The data were computed after Fukushima (2017) at the nodes of the Gauss–Legendre grid corresponding to degree 225 ( $226 \times 452$  points). The grid residing on the Bennu’s surface  $S$  is actually 0.01 m above  $S$  to ensure harmonicity of the gravitational potential. The radii of the mean and the Brillouin spheres are given in Table 1. Each of the three grids is based on point values of the reference gravitational potential. Therefore, all validations using these data that follow are based on point values as well

Vertical position of the grid	min ( $\text{m}^2 \text{s}^{-2}$ )	max ( $\text{m}^2 \text{s}^{-2}$ )	mean ( $\text{m}^2 \text{s}^{-2}$ )	STD ( $\text{m}^2 \text{s}^{-2}$ )	RMS ( $\text{m}^2 \text{s}^{-2}$ )
Bennu’s surface $S$	1.939E-2	2.252E-2	2.128E-2	5.845E-4	2.129E-2
Mean sphere $\bar{\Omega}$	2.064E-2	2.229E-2	2.118E-2	3.945E-4	2.118E-2
Brillouin sphere $\bar{\Omega}$	1.804E-2	1.935E-2	1.840E-2	2.854E-4	1.841E-2

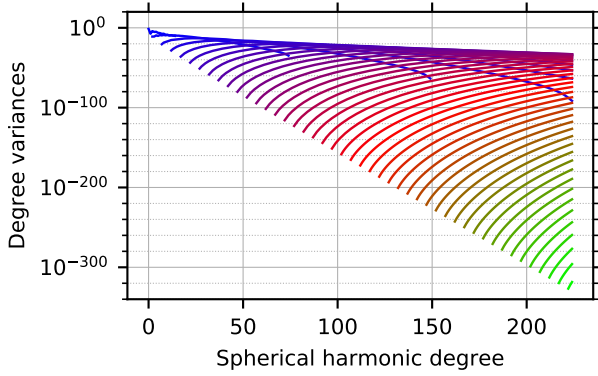


**Fig. 6** Spectra (dimensionless) of the gravitational contributions to  $V_{\text{res}}^{\text{SGFM}}$  (Eq. 9) made by  $H^p$  with  $p$  varying from 1 (light blue colour) to 228 (light green colour). For visualization purposes, shown are only the powers  $p = 1, 5, 10, 15, \dots$ . The degree variances are referenced to the Brillouin sphere  $\bar{\Omega}$ . The sum of all contributions yields the degree variances from Fig. 5 (the Brillouin sphere case). For visualization purposes, the original coefficients in quadruple precision are used to avoid underflow

Comparing the figure with the Bennu’s shape (Fig. 2), the worst results are generally seen over low-elevated topography, which is deep inside the sphere of convergence. On the other hand, still relatively good agreement of 10 or more digits is achieved over high-elevated regions that are closer to the sphere of convergence.

In Fig. 9, errors of spectral gravity forward modelling are shown as a function of the maximum harmonic degree  $N_{\text{SGFM}}$ . This may help us in addressing the three topics discussed in the last paragraph of Section 3.1.

1. Recalling the Footnote 2 from Page 5, the orange curve implies that this particular spherical harmonic series may indeed be considered as asymptotic when evaluated on the Bennu’s surface. This, however, is possible only within some limited accuracy level, here  $\sim 10^{-5} \text{ m}^2 \text{s}^{-2}$  in terms of the standard deviation which roughly corresponds to  $\sim 3 - 4$  correct digits. This minimum is attained at harmonic degree  $\sim 25$ .

Therefore, when using the term asymptotic series in relation to convergence/divergence of spherical harmonics on planetary topographies, we recommend to always specify an estimation of the best possible accuracy that can be achieved with the series and to accompany the es-

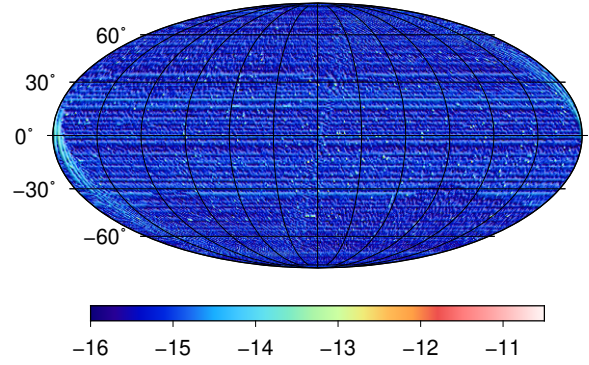


**Fig. 7** Validation of spectral gravity forward modelling on the Brillouin sphere via  $\log_{10}(\delta V)$  (Eq. 24). The grid nodes are given by the Gauss–Legendre quadrature (degree 225) and the potential  $V^{\text{SGFM}}$  is synthesized up to degree  $N_{\text{SGFM}} = 225$ . The value of  $-16$  indicates the maximum possible 16-digit agreement (double precision). At 99.4 % of the points, it holds that  $\log_{10}(\delta V) \leq -14$

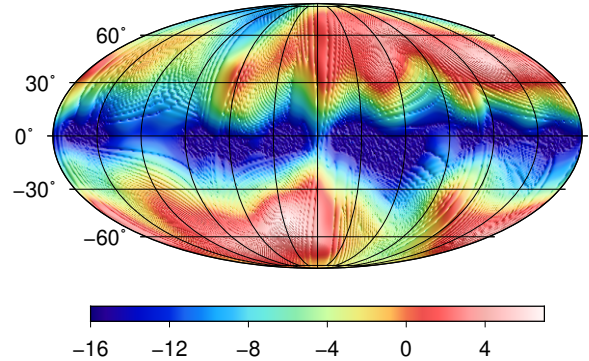


**Fig. 8** Same as Fig. 7 but on the Bennu’s surface. The spherical harmonic synthesis was done by the exact point-wise algorithm, avoiding the more efficient but less accurate gradient approach of, e.g., Balmino et al (2012) and Hirt (2012). The same approach is followed throughout the paper whenever we synthesize the gravitational potential on the Bennu’s surface  $S$

timation by the associated truncation degree. Otherwise, justifying the use of spherical harmonics (Eq. 8 and its variations) below the sphere of convergence by referring to the asymptotic-type of series may be misleading. This is because the series may not have the capability to represent the gravitational potential within the accuracy required by the user. As a rule of thumb, the best accuracy

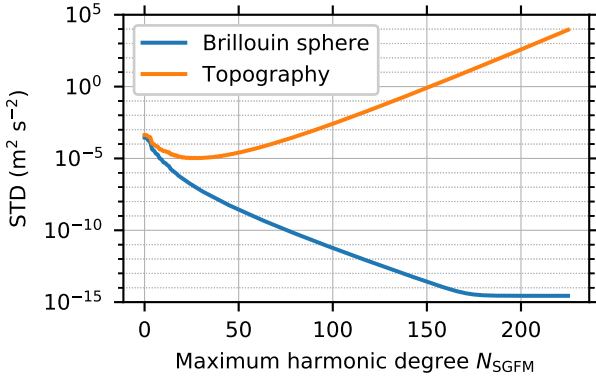


**Fig. 9** Errors of spectral gravity forward modelling in terms of the standard deviation (STD) as a function of  $N_{\text{SGFM}}$  ( $p_{\text{max}}$  fixed to 228). The same evaluation points as in Fig. 7 and 8 are used. After degree  $\sim 175$ , the blue curve remains nearly on the same level, implying that the numerical limitations of the double precision environment have been reached

that can be obtained on the body’s surface with Eq. (8) seems to decrease with the complexity of the body (represented, for instance, by the shape ratio among other possible parameters).

2. Based on the previous comment, it becomes clear that even though the series is always finite in practice, the issue of its convergence/divergence on the body’s surface may indeed be a problem, especially if a suitable analysis of the series was not conducted prior to its usage.
3. A similar conclusion is drawn in relation to the third comment from the last paragraph of Section 3.1. Despite that the series (8) is always finite in practice, and thereby always yields finite values everywhere above the body, using it to represent the reference gravitational potential for gravity observations on the body’s surface may be rather dangerous without knowing a suitable truncation degree as is clear from Fig. 9.

Naturally, the comments from the last paragraph of Section 3.1 were made in the context of the Earth’s gravitational field, which is less prone to the series divergence (see Introduction). In that case, Eq. (8) may be sufficiently accurate for many current applications, even on the Earth’s surface, and the accuracy can be retained up to higher degrees than shown in Fig. 9. Nonetheless, since the series is infinite in theory, it seems that one will face sooner or later the same issues, although only after reaching some sufficiently high harmonic degrees. Recent studies show that for the Earth’s gravitational field and a  $\mu\text{Gal}$  accuracy level, the turning point can be expected around degree 10,800 (or perhaps even sooner) (e.g., Hirt et al, 2016; Bucha et al, 2019b; Rexer, 2017).

**Table 3** CPU time needed to evaluate the right-hand side of Eq. (10) using the numerical integration technique of Fukushima (2017). In all cases, the maximum degree is  $N_{\text{LS}} = 65$  and the computations were conducted in double precision. To compute the left-hand side of Eq. (10), we use throughout the paper the relative error tolerance of  $\delta = 10^{-16}$

$\delta$	CPU time (years)
$10^{-8}$	16
$10^{-10}$	25
$10^{-12}$	50

#### 4.3 Least-squares estimation from surface gravitational data

This section numerically investigates the least-squares method from Section 3.2. The main underlying research question is whether it can approximate the gravitational data on the Bennu’s surface  $S$  more accurately than spectral gravity forward modelling (Section 4.2), that is, to lower the minimum error threshold of  $\sim 10^{-5} \text{ m}^2 \text{ s}^{-2}$  (cf. the orange curve in Fig. 9).

In order for  $V^{\text{LS}}$  from Eq. (13) to accurately represent the reference potential  $V^{\text{Ref}}$  on  $S$ , we found two aspects that are essential.

1. *Accurate evaluation of the scalar products from Eq. (10).* Due to the positive experience with the numerical integration after Fukushima (2017) from Sections 4.1 and 4.2 (Fig. 7), we employed the method to evaluate the scalar products from Eq. (10), too. For the right-hand side of the equation, this means coping with quadruple integrals (one double integral for  $V$ , another for the scalar product), each of which we separately compute by our modification of the `dqde.f90` subroutine. Three values of the relative error tolerance parameter  $\delta$  are used in order to study the impact of the numerical accuracy of the linear system (10) on the output potential  $V^{\text{LS}}$  (Table 3). The method of Fukushima (2017) was applied also to the left-hand side of Eq. (10), where double integrals occur. Even though there is a significantly larger number of scalar products on this side of the equation, its computation is faster, because  $\bar{S}_{nm}$  is much easier to evaluate than  $V$  (cf. Eq. 11). This time, we therefore use only a single low relative error tolerance of  $10^{-16}$ .

2. *Sufficiently high  $N_{\text{LS}}$ .* Limited by the computational power, we set the maximum harmonic degree  $N_{\text{LS}}$  to 65. Despite this seemingly low degree, it suffices for spectral gravity forward modelling to notably diverge (see Fig. 9), so the superiority of least-squares solutions may be identified if any. The computations related to this numerical experiment took  $\sim 90$  CPU years combined and were conducted using 400 CPUs (see Table 3).

After computing all the scalar products from Eq. (10) in Fortran, we read the results in Python and solve the

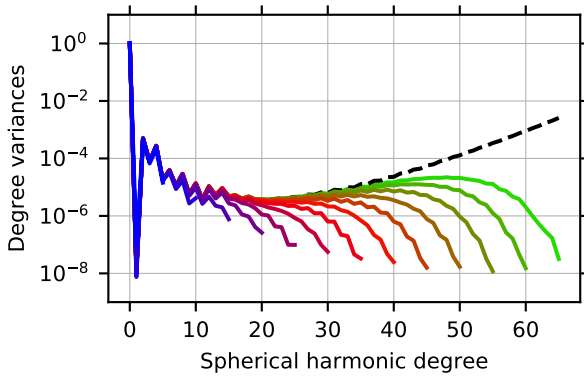


**Fig. 10** Spectrum (dimensionless) of the least-squares solutions  $V_{LS}$  estimated up to degrees  $N_{LS} = 5$  (blue colour),  $10, \dots, 65$  (light green colour). For visualization purposes, the solution for  $N_{LS} = 0$  is not shown (a single dot coinciding with all the curves at degree 0). The dashed black line shows the spectrum of  $V_{SGFM}$  (the same as the blue line from Fig. 5 but this time including  $V_{ball}$ , see Eq. 2). The degree variances refer to the Bjerhammar sphere

linear system using the SciPy's `scipy.linalg.solve` routine (Virtanen et al, 2020) with the `assume_a='pos'` flag (positive-definite normal equations matrix). The SciPy module relies on LAPACK (Anderson et al, 1999).

Having the linear system of equations (10) up to degree 65, we estimated 14 least-squares solutions, each with a different maximum degree  $N_{LS} = 0, 5, 10, \dots, 65$ . This is done so as to study the impact of  $N_{LS}$  on  $V_{LS}$  and  $\bar{V}_{nm}^{LS}(N_{LS})$  (see Section 3.2).

In Fig. 10, we show the spectra of the obtained models (the colour lines). They are significantly different from spectral gravity forward modelling (the dashed black line) which should not be surprising, despite the fact that both methods describe the same external gravitational field. This is because the least-squares solutions can accurately reproduce the gravitational field even below the sphere of convergence (but outside the body), which is generally not true for spectral gravity forward modelling. This difference must therefore somehow translate into the coefficients, causing their conceptual inconsistency (Sacerdote and Sansò, 2010; Sansò and Sideris, 2013; Bucha et al, 2019c).

The figure also reveals a strong dependence of the least-squares solutions on  $N_{LS}$ . More specifically, as  $N_{LS}$  increases, the solutions start to more and more adhere the *divergent* series from spectral forward modelling. After some critical degree, however, the spectra decline significantly unlike the divergent solution, which continues in gaining more and more signal power. We believe this distinct behaviour is the consequence of the coefficients inconsistency.

To better illustrate the differences between the least-squares solutions and spectral gravity forward modelling, we plotted in Fig. 11 their difference degree variances. From Eq. (14), they should decrease with increasing  $N_{LS}$  which is exactly what is seen in the figure. The situation is slightly

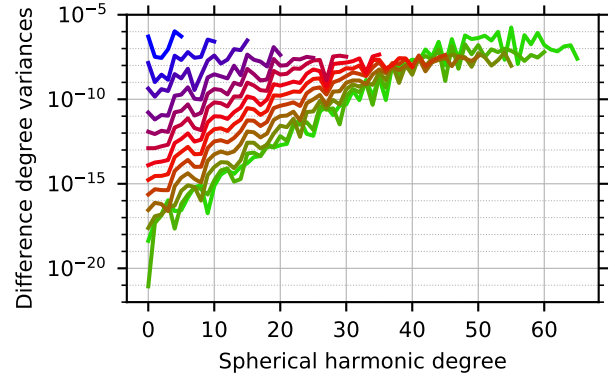


**Fig. 11** Difference degree variances (dimensionless) between the solutions from the least-squares method (colour lines in Fig. 10) and from spectral gravity forward modelling (the black dashed line in Fig. 10). The same colour scheme as in Fig. 10 is used

less clearly only for two solutions with the highest  $N_{LS}$  (60 and 65, light green lines), for which the curves start to oscillate beyond degree  $\sim 30$ . This behaviour might indicate that the two solutions are getting close to limitations caused by the restricted computational accuracy that was used to deliver the linear system (10) (see Table 3). To our knowledge, Fig. 11 is the first indirect numerical confirmation of Eq. (14).

Next, in Fig. 12, we validate the least-squares models in the spatial domain on the surface of Bennu, and compare the results with spectral gravity forward modelling. The figure shows that the least-squares models can be significantly superior to (divergent) spectral gravity forward modelling, for instance, more than 3 orders of magnitude when  $N_{LS} = 65$ . Clearly visible is also the positive effect of increasing  $N_{LS}$  which mitigates the errors when the models are evaluated up to their maximum degrees  $N_{LS}$  (the solid black line in Fig. 12).

Similarly as with the degree variances from Fig. 10, the standard deviations in Fig. 12 tend to closely follow the errors of divergent spectral forward modelling, but, after some degree, they significantly drop. These last few degrees are crucial, as they boost the performance of the least-squares models. Of great importance is also the fact that the standard deviations do not necessarily decrease monotonically. In other words, partial sums up to degree  $n < N_{LS}$  may produce worse results than partial sums up to  $n - 1$ . We will refer to this behaviour as the *divergence effect* (which is not to be confused with the divergence of an infinite series; see Section 4.2.6 of Bucha et al, 2019b). Taking the solution with  $N_{LS} = 65$  as an example, the divergence effect was observed for 20 pairs of successive harmonic degrees.

These results lead to an observation, which—should it not be supported by the theory from Section 3.2 and the numerical experiments—might sound as self-conflicting. On the one hand, if we increase  $N_{LS}$  and the numerical accuracy

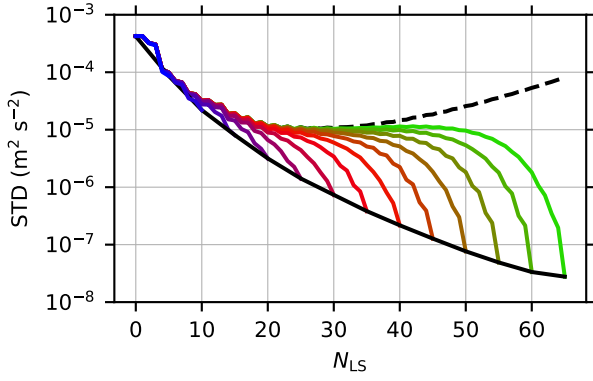


**Fig. 12** Validation of the least-squares models on the Bennu's surface in terms of the standard deviation (STD). The colour lines show standard deviations for the least-squares models developed with  $N_{LS} = 5$  (blue colour), 10, ..., 65 (light green colour), each one being evaluated as partial sums gradually up to degrees 0, 1, 2, ...,  $N_{LS}$ . The solid black line represents the standard deviations for each least-squares model when it is evaluated up to its maximum harmonic degree (including the  $N_{LS} = 0$  solution). For a comparison, the dashed black line shows the errors of spectral gravity forward modelling (the orange curve from Fig. 9). The standard deviations were obtained from data given at the nodes of the Gauss–Legendre quadrature for degree 225 (oversampling factor of  $\sim 3.5$  for  $N_{LS} = 65$  and higher for the other models). The reference data were taken from Table 2

of the linear system (10), we get better and better approximation of the surface gravitational data, just as it is expected based on the Runge–Krupp theorem. This statement is supported by Figs. 12 (the solid black line) and 13. Yet, on the other hand, the spherical harmonic coefficients approach the coefficients from the series (8) (see Figs. 10 and 11), which, in our case study, is *divergent* for surface gravitational data (see the orange curve in Fig. 9). As a result, the divergence effect of partial sums is likely to amplify with increasing  $N_{LS}$ . Some consequences of this behaviour will be discussed in Section 5.

As the last validation on the surface of Bennu, Fig. 14 compares the least-squares solution for  $N_{LS} = 65$  with the reference data. The figure shows the  $\log_{10}(\delta V)$  measure from Eq. (24) but for  $V^{LS}$  instead of  $V^{SGFM}$ . Typically, the figure shows small errors over deep valleys, while large errors (in a relative sense) are seen over high-elevated topography (cf. Fig. 2). This is the opposite behaviour as could be seen in Fig. 8 with spectral gravity forward modelling. A possible explanation might be that the low-elevated topography is close to the Bjerhammar sphere, to which the data are downward continued during the least-squares estimation. Due to the short continuation distances, only small errors are therefore introduced. The exact opposite is true for hills, which are associated with long downward continuation distances, hence large errors in the relative sense.

To draw a more complete picture on the behaviour of the least-squares models in the spatial domain, we repeated the validation but with evaluation points on a Brillouin sphere

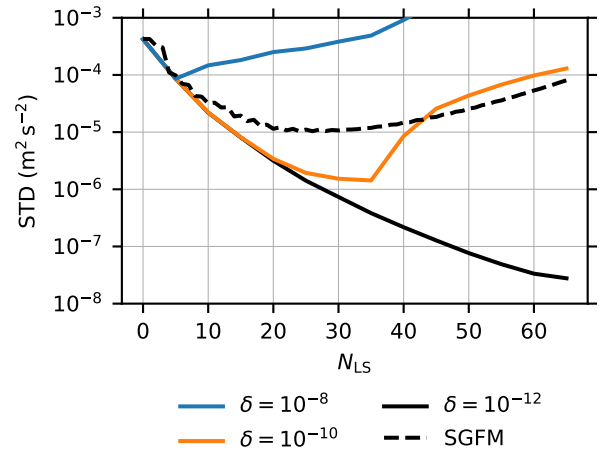


**Fig. 13** Effect of the relative error tolerance  $\delta$  on the right-hand side of Eq. (10). The least-squares models were estimated for  $N_{LS} = 0, 5, \dots, 65$ . For each model, the potential was synthesized using the full model, that is, with its maximum degree  $N_{LS}$ . The solid black line is therefore identical to that in Fig. 12. For a comparison, the dashed black line from Fig. 12 (spectral gravity forward modelling) is shown, too. In all cases, the left-hand side is evaluated with  $\delta = 10^{-16}$ . Besides this figure, all other results presented in the paper rely on  $\delta = 10^{-12}$  on the right-hand side of Eq. (10)

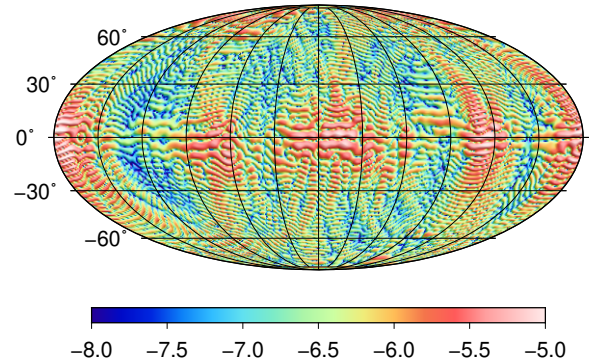


**Fig. 14** Validation of the least-squares solution with  $N_{LS} = 65$  on the surface of Bennu in terms of  $\log_{10}(\delta V)$  (Eq. 24). The synthesis was performed up to the maximum degree  $N_{LS} = 65$  and both the grid nodes and the reference potential are the same as in Fig. 8

(Fig. 15). Similarly as on the Bennu's surface, the model errors decrease with increasing  $N_{LS}$  (the solid black line). Similar is also the fact that, up to certain degree, the standard deviations closely copy the accuracy of spectral gravity forward modelling. After some critical degree, however, we see the standard deviations remaining nearly on the same level (the almost horizontal colour lines). While these last few degrees were substantial on the surface of Bennu (see Fig. 12), they do not seem to bring any significant improvement on the Brillouin sphere. In fact, above the sphere of convergence, the least-squares solutions converge slower than spectral gravity forward modelling (compare the solid and dashed black lines in Fig. 15). Finally, we acknowledge that the standard deviations decrease monotonically over the



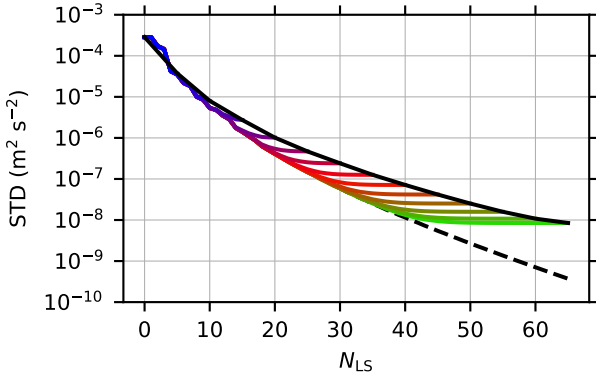


**Fig. 15** The same as Fig. 12, but on the Brillouin sphere from Table 1. The dashed black line represents spectral gravity forward modelling (a part of the blue curve from Fig. 9)

entire studied bandwidth which is in accordance with the theory.

#### 4.4 Internal and external series expansions

In agreement with Section 3.3, the gravitational field is studied only on the mean sphere  $\Omega$  in this section. The radius of the sphere is reported in Table 1. We recall that the gravitational potential is harmonic whenever the sphere passes through the mass-free space and non-harmonic otherwise.

We use the following values of the truncation parameters from Eqs. (17) – (20),  $N_{\text{Ext}} = N_{\text{Int}} = 450$  and  $p_{\text{max}}^{\text{Ext}} = p_{\text{max}}^{\text{Int}} = 1000$ . Similarly as in Section 4.2, we use the Gauss–Legendre quadrature for spherical harmonic analysis of  $H^{(rs \leq R)}$  and  $H^{(rs \geq R)}$ . But since the functions are non-band-limited (see Section 3.3), the quadrature is no longer exact. Therefore, we computed the coefficients up to degree 2160, but only the ones up to degree 450 will be used to synthesize the gravitational potential. This is done so as to diminish the aliasing effect. To further narrow computational errors, the entire spherical harmonic analysis as well as the evaluation of  $\bar{V}_{nm}^{\text{Ext}}$  and  $\bar{V}_{nm}^{\text{Int}}$  was performed in quadruple precision. The final coefficients were obtained after a conversion to double precision. The gravitational potential is finally synthesised in double precision, similarly as with all the previous methods.

In Fig. 16, we show the spectra of  $V_{\text{res}}^{\text{IE}}$  from Eq. (16) for several values of  $p_{\text{max}}^{\text{Ext}} = p_{\text{max}}^{\text{Int}}$ . The figure reveals that a large number of topography powers may be needed to achieve the convergence at a reasonable degree of the numerical approximation. This is obvious from the wave-like feature that is present in the depicted spectral bandwidth if  $p_{\text{max}}^{\text{Ext}} = p_{\text{max}}^{\text{Int}} \approx 200$  (beyond this power, the wave is no longer visible at this scale). With increasing  $p_{\text{max}}^{\text{Ext}}$  and  $p_{\text{max}}^{\text{Int}}$ , the wave moves towards higher harmonic degrees and its amplitude grows significantly which clearly demonstrates the necessity of using high topography powers. To further investigate the wave-

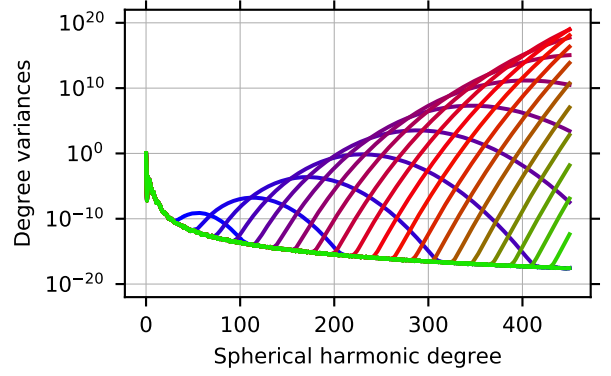


**Fig. 16** Degree variances (dimensionless) of  $V_{\text{res}}^{\text{IE}} = V^{\text{Ext}} + V^{\text{Int}}$  plotted from the  $\bar{V}_{nm}^{\text{Ext}}(R) + \bar{V}_{nm}^{\text{Int}}(R)$  coefficients up to degree 450. The curves show the spectrum at various levels of its completeness in terms of  $p_{\text{max}}^{\text{Ext}} = p_{\text{max}}^{\text{Int}} = 10$  (blue curve), 20, 30, ..., 200, 1000 (green curve). Note that for the last curve with  $p_{\text{max}}^{\text{Ext}} = p_{\text{max}}^{\text{Int}} = 1000$  (as well as for any  $p_{\text{max}}^{\text{Ext}} = p_{\text{max}}^{\text{Int}} > 200$ , not shown in the figure), no wave-like feature is visible within the studied bandwidth. The coefficients  $\bar{V}_{nm}^{\text{Ext}}(R) + \bar{V}_{nm}^{\text{Int}}(R)$  were summed in quadruple precision to avoid underflow

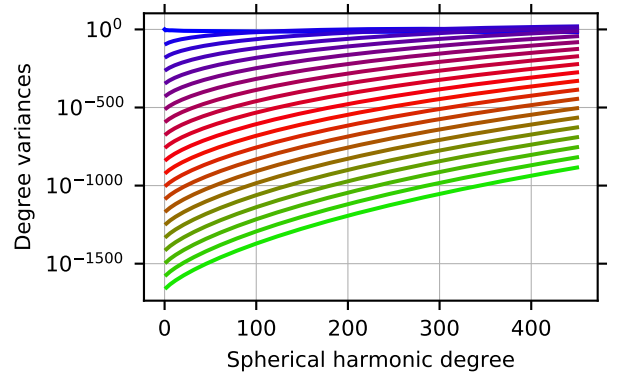


**Fig. 17** Spectra (dimensionless) of the gravitational contributions to  $V^{\text{Int}}$  made by the  $p$ th powers of  $H^{(rs \geq R)}$  with  $p = 1$  (blue colour), 50, 100, ..., 1000 (green colour). The spectra are shown up to degree 450 and refer to the mean sphere  $\Omega$ . To avoid underflow, the quadruple version of the coefficients was used to prepare the figure

like feature, we split  $V_{\text{res}}^{\text{IE}}$  into  $V^{\text{Int}} + V^{\text{Ext}}$  (see Eq. 16) and show in Figs. 17 and 18 the gravitational contributions of the powers  $p$  made to  $\bar{V}_{nm}^{\text{Int}}(R)$  and  $\bar{V}_{nm}^{\text{Ext}}(R)$ , respectively (Eqs. 20 and 18). For instance, at harmonic degree 450, the signal degree variance for  $V^{\text{Int}}$  reaches  $\sim 10^{-170}$  when  $p = 450$ , whereas  $V^{\text{Ext}}$  is only at the order of  $\sim 10^{-740}$  for the same  $p$ . This demonstrates that the vast portion of the wave stems from the binomial expansion of  $\bar{V}_{nm}^{\text{Int}}$  from Eq. (20). Some related discussion on the convergence properties of the involved binomials expansions can be found, for instance, in Sun and Sjöberg (2001).

In Fig. 19, we validate the combination of internal and external series expansions with respect to the reference gravitational potential obtained by the method of Fukushima (2017) (see Table 2). The figure shows the importance of using sufficiently high number of topography powers in

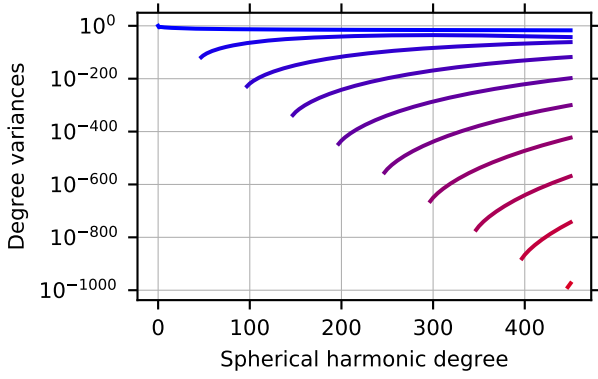


**Fig. 18** Spectra (dimensionless) of the gravitational contributions to  $V^{\text{Ext}}$  made by the  $p$ th powers of  $H^{(rs \leq R)}$  with  $p = 1$  (blue colour), 50, 100, ..., 450 (red colour). The same colour scheme is used as in Fig. 17. Note that the powers  $p > 453$  no longer contribute to the gravitational potential within the studied harmonic degrees (see Section 4.2). The spectra are shown up to degree 450 and refer to the mean sphere  $\Omega$ . To avoid underflow, the quadruple version of the coefficients was used to prepare the figure

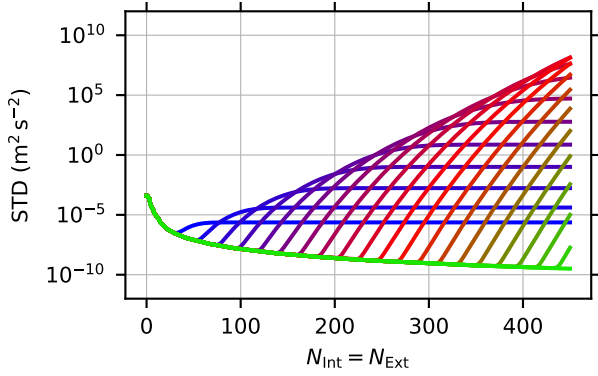


**Fig. 19** Validation of the internal and external series expansions against the reference gravitational potential on the mean sphere  $\Omega$ . The standard deviations (STDs) of the discrepancies are shown for  $p_{\text{max}}^{\text{Int}} = p_{\text{max}}^{\text{Ext}} = 10$  (blue colour), 20, 30, ..., 200, 1000 (green colour) as partial sums with increasing  $N_{\text{Ext}} = N_{\text{Int}} = 0, 1, 2, \dots, 450$ . The reference data were taken from Table 2

Eqs. (18) and (19) in order to achieve convergence numerically. Obviously, it is the wave-like feature from Fig. 16 that deteriorates the results if  $p_{\text{max}}^{\text{Int}}$  and  $p_{\text{max}}^{\text{Ext}}$  are too low (here below  $\sim 200$ ). Fig. 20 shows the standard deviation as a function of  $p_{\text{max}}^{\text{Ext}} = p_{\text{max}}^{\text{Int}}$  with several values of  $N_{\text{Ext}} = N_{\text{Int}}$ . The two figures indicate that to further decrease the errors, we should rather increase  $N_{\text{Ext}} = N_{\text{Int}}$  beyond degree 450 instead of reaching  $p_{\text{max}}^{\text{Ext}} = p_{\text{max}}^{\text{Int}}$  beyond 1000. This, however, is computationally challenging, as it requires to move from quadruple to some higher precision when computing Eqs. (18) and (19) and all their terms. In addition, the synthesis of the gravitational potential might also need to be conducted using the extended precision.

Next, Fig. 21 plots the spatial distribution of the errors on the mean sphere. It shows that the largest errors occur in the vicinity of the intersections of the mean sphere  $\Omega$

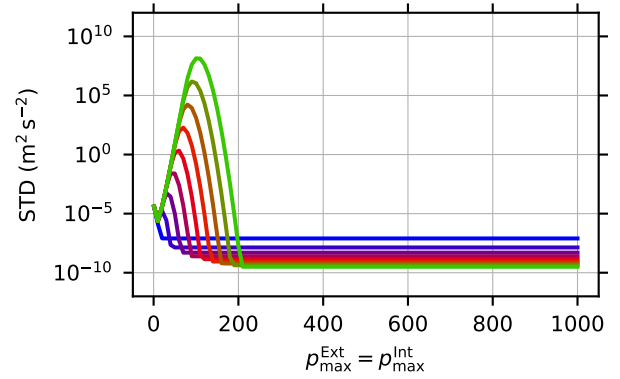


**Fig. 20** Validation of the internal and external series expansions on the mean sphere as a function of  $p_{\text{max}}^{\text{Int}} = p_{\text{max}}^{\text{Ext}}$  with  $N_{\text{Ext}} = N_{\text{Int}} = 50$  (the blue colour), 100, ..., 450 (the green colour). The following values of  $p_{\text{max}}^{\text{Int}} = p_{\text{max}}^{\text{Ext}}$  were used: 1, 10, 20, ..., 250, 300, 400, 500, 750 and 1000. The reference data were taken from Table 2

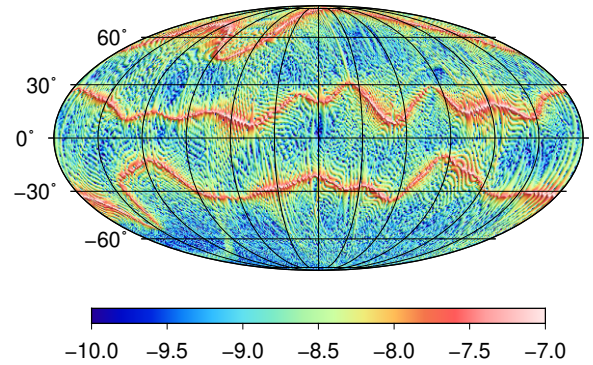


**Fig. 21** Validation of the internal and external series expansions on the mean sphere using  $\log_{10}(\delta V)$  from Eq. (24). The synthesis was performed up to degree  $N_{\text{Ext}} = N_{\text{Int}} = 450$  with  $p_{\text{max}}^{\text{Int}} = p_{\text{max}}^{\text{Ext}} = 1000$ . The reference data were taken from Table 2. Note that some values exceed the scale of the colour bar. The true range is from about  $-13.6$  to  $-6.5$

with the surface of Bennu  $S$ , where the gravitational potential changes its harmonicity from harmonic to non-harmonic (or vice versa). It therefore appears, especially also in relation to Figs. 19 and 20, that a larger number of spherical harmonics is needed to capture the transition zone more accurately.

As a final validation, we compare the combination of internal and external expansions with the two previous methods. Ideally, this would be done on the Bennu's surface, similarly as in the previous sections. But since the coefficients from Eqs. (17) and (19) depend on the radius of the evaluation point, an accurate computation is demanding (for a possible approximate solution, see, e.g., Górski et al, 2018). Therefore, we provide in Fig. 22 a validation on the mean sphere. This time, however, the potential is synthesized only on those parts of the mean sphere that are in the mass-free space, where the gravitational potential is harmonic. In this region, all the studied methods can provide accurate results

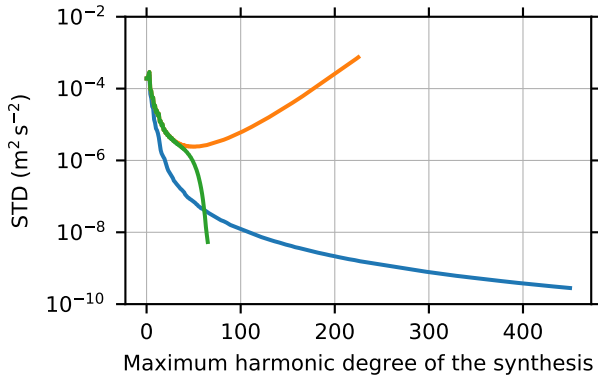


**Fig. 22** Validation of the studied techniques on the parts of the mean sphere that are external to the body: spectral gravity forward modelling (orange curve,  $N_{\text{SGFM}}$  up to 225), least-squares estimation (green curve,  $N_{\text{LS}}$  up to 65), and the combination of internal and external series expansions (blue curve,  $N_{\text{Ext}} = N_{\text{Int}}$  up to 225,  $p_{\text{max}}^{\text{Int}} = p_{\text{max}}^{\text{Ext}} = 1000$ ). The reference data were taken from Table 2

except for spectral gravity forward modelling. The figure shows that for maximum harmonic degree 65, which is the highest degree available in all our models, the lowest standard deviation was achieved with the model from the least-squares method. To what extent this observation can be generalized to some conclusions related to the studied methods is, however, not known to us presently. Further studies are necessary to reveal whether this can be considered as a typical behaviour or not.

## 5 Discussion

Motivated by the widespread use of spherical harmonics for gravitational field modelling near the Earth’s surface, we studied convergence/divergence properties of three spherical-harmonic-based techniques. Our experiment was designed to simulate—at least partially—properties that may be expected to be observed on the Earth after reaching sufficiently high degree of the expansion. To lower the computational complexity, we worked with a strongly irregular body, the Bennu asteroid. The asteroid offers serious divergence effect already at degrees beyond  $\sim 25$  which makes it a suitable object for the experiment. We believe that our study sheds some new light on some of the open questions that are associated with the inconsistency of spherical harmonic coefficients from satellite (Section 3.1) and terrestrial data (Sections 3.2).

Let us start with the second open issue from Section 68.5 of Sacerdote and Sansò (2010):

*“Up to what degree is it sensible to push such procedures, i.e. is the maximum degree  $N$  bounded only*

*by our computing capacity or should we limit it for practical reasons?”<sup>5</sup>*

Section 4.3 suggests that for the best fit of surface gravitational data, the maximum degree should be as high as possible (see Fig. 12), being bounded only by the computing capacity and/or data availability. However, hand in hand with the increasing maximum degree must go an improvement of the input data accuracy; otherwise, the results may be useless (see Fig. 13). As shown in our numerical experiments, this is difficult to satisfy even in a well-defined simulation study, where all input data can be computed on demand (see the computation times in Table 3). Another important aspect is that larger and larger portion of the spectrum approaches the (possibly divergent) traditional spherical harmonic series as we increase the maximum harmonic degree (see Eq. 14 and Figs. 10 and 11). In practical applications, this may have serious consequences, for instance, if partial sums are evaluated below the sphere of convergence (see Fig. 12). In that case, one may observe the divergence effect of partial sums, which may completely prevent the use of such model in the applications discussed in the second paragraph of Introduction. The divergence effect of partial sums therefore implies that there may indeed be some practical reasons for limiting the maximum degree. To our understanding, the answer to the formulated question therefore depends on the intended purpose of the model to be estimated.

Our numerical experiments may provide also an answer to the second research question formulated by Bucha et al (2019c) in their Section 5. In our notation, it can be formulated as follows. Assume two models of  $V^{\text{LS}}$  (Eq. 13), each estimated up to a different harmonic degree,  $N_{\text{LS},1}$  and  $N_{\text{LS},2} > N_{\text{LS},1}$ . The question is what approximation errors of partial sums can be expected when the two models are synthesized up to some degree  $N_{\text{LS},3}$  that is common to both models,  $N_{\text{LS},3} \leq N_{\text{LS},1} < N_{\text{LS},2}$ . Fig. 12 clearly shows that the model with the *higher* maximum degree, here  $N_{\text{LS},2}$ , may yield a worse approximation of the surface gravitational data. This indicates that when computation points reside on the body’s surface (more precisely, below the sphere of convergence), models from terrestrial gravitational data should be evaluated in most cases up to their maximum harmonic degree, avoiding the use of partial sums that may suffer from the divergence effect. Opposed to this, when the target area is above the sphere of convergence, Fig. 15 implies that the model with  $N_{\text{LS},2}$  always outperform that with  $N_{\text{LS},1}$ , be it for partial sums evaluated up to  $N_{\text{LS},3}$  or for the full models.

The present study might also provide some hints in relation to the first research question from Section 5 of Bucha et al (2019c), although with less confidence due to the lack of specifically tailored experiments. The issue is what errors

<sup>5</sup> In our study,  $N_{\text{LS}}$  plays the role of  $N$  from Sacerdote and Sansò (2010).



can be expected when combining the coefficients from satellite data (Section 4.2) with that from terrestrial data (Sections 4.3). In practice, this is seen with combined spherical-harmonic-based models such as EGM2008. Based on the results from Section 4, we expect that this may cause the coefficients to be closer to the (possibly divergent) traditional spherical harmonic series (similarly as in Fig. 11), thereby yielding stronger divergence effect of partial sums, yet the model will provide a better fit of the gravitational data when used up to its maximum harmonic degree (similarly as in Fig. 13). Even though this expectation is partially indicated by the numerical results, it must be understood as an unverified statement that needs to be further examined both theoretically and numerically.

## 6 Conclusions

We have numerically demonstrated that the gravitational potential of a complex asteroid (101955) Bennu can be reproduced with the relative error of  $10^{-6}$  everywhere on its surface and above it even when using a single truncated external spherical harmonic series only. The results are supported by the Runge–Krarup theorem and perhaps might sound pleasingly in relation to near-surface applications of the Earth’s spherical-harmonic-based gravitational models. The paper, however, outlined also some practical limitations of this approach.

Our results indicate that the models of the Runge–Krarup-type should be synthesized exclusively up to their maximum harmonic degrees. Otherwise, one risks the divergence effect of partial sums. Unfortunately, this implies that the spectral decomposition of the gravitational field—considered by us as one of the essential properties of spherical harmonics—is significantly limited with such models, at least below the sphere of convergence. As another drawback, an accurate determination of such models is a computationally difficult task, even after simplifying the gravitating object in terms of its geometry and density. In fact, these postulations were essential for us to diminish various kinds of errors.

The paper also numerically shows that the divergence effect can be avoided if external spherical-harmonic-based modelling is replaced by a combination of internal and external series expansions. This technique is known for decades in the geodetic literature, yet its applications are somewhat modest. This could be because it requires a knowledge of the geometry and density of the Earth, the latter of which is problematic, causing the models to be less accurate and detailed than that relying on measured gravitational data.

For the time being, practitioners in geosciences may not need to be disturbed by the herein presented results. This is simply because the accuracy and density of our terrestrial gravity data sets are still so poor (or excellent, depending

on the context) that many of the troublesome effects seen in our study have not yet been observed with real data. Or, in simple words, our current real-world conditions might allow us to reach the level of the blue or purple curves in Fig. 12, whereas notable differences start to be observer only with, say, the red and green curves, which are beyond our current imagination. Regardless of whether or not we may ever be able to reach this level in the real world, numerical experiments of this kind as well as theoretical discussions on these topics are necessary, simply to allow us to better understand the techniques we exploit on a daily basis.

At any rate, whether one decides for the least-squares method or for the combination of internal and external series expansions, the common factor is that their expansion coefficients are no longer constant, but instead depend on some variable. In the first method, the coefficients depend on the maximum degree of the spherical harmonic series, whereas in the second method, the argument is the radius of the evaluation point. Regarding the least-squares method (and the Runge–Krarup-type models in general), we think it is this dependence that vanishes some of the powerful features of external spherical harmonics when applied below the sphere of convergence, making it somewhat closer to the abilities of spatial-domain methods.

Finally, we would like to acknowledge that the change of boundary approach (e.g., Sansò, 1993; Sansò and Sideris, 2013, 2017; Pavlis et al, 2012) appears to be another method suitable to deliver external spherical-harmonic-based models from surface gravitational data. These models are conceptually similar to that from the studied least-squares technique in the sense that they also aim to reproduce surface gravitational data and their coefficients depend on the maximum degree of the expansion. Following Bucha et al (2019c), we studied this technique within the closed-loop environment from this paper, too. However, since the gravitational field of Bennu is rather complex, we switched from using point values of the input surface potential to mean values. The approach based on mean values has already been applied in the literature (though under less challenging numerical conditions; e.g., Pavlis et al, 2012), but we have noticed that it is extremely difficult, at least for us, to apply it in such a way that it can compete with the herein presented least-squares models in terms of accuracy. In our implementation, the change of boundary method converges too slowly when mean values are used. At the same time, the method is too complex numerically, so it is difficult to increase the resolution of the input surface potential in order to improve the final accuracy. For complex bodies and their gravitational fields, this point is therefore left open for the time being.

**Author contributions:** BB designed the study, conducted all numerical experiments and drafted the manuscript. FS improved the design

of the numerical experiments and refined the theoretical background of the study. BB and FS discussed and commented on the manuscript.

**Data availability:** The input polyhedral model of the Benu's shape is available at <https://sbn.psi.edu/pds/resource/bennushape.html>. The data produced within this study are available at <http://edisk.cvt.stuba.sk/~xbuchab/>. These include: (i) the  $\bar{r}_{nm}^S$  coefficients from Eq. (1), (ii) spherical harmonic coefficients of  $V^{SGFM}$  from Eq. (2) (including the effect of the  $V_{ball}$  term), (iii) the  $\bar{V}_{nm}^{LS}(N_{LS})$  coefficients from Eq. (13) for  $N_{LS} = 0, 5, 10, \dots, 65$ , (iv) the  $\bar{V}_{nm}^{Ext}$  and  $\bar{V}_{nm}^{Int}$  coefficients computed with  $p_{max}^{Int} = p_{max}^{Ext} = 1000$ , (v) the three grids of the reference gravitational potential from Table 2, and (vi) the GFM\_DE\_rule package for spatial-domain gravity forward modelling (Fortran and MATLAB) after Fukushima (2017). Due to their size (~17.5 GB), the scalar products from Eq. (10) were not uploaded, but are available on the request from BB. Other (already published) routines that were used in this study, particularly for ultra-high-degree spherical harmonic analysis and synthesis (Fortran, C and MATLAB), are also available at the latter link.

**Acknowledgements** The computations were performed at the HPC centres at the Slovak University of Technology in Bratislava, the Slovak Academy of Sciences and the University of Žilina, which are parts of the Slovak Infrastructure of High Performance Computing (SIVVP project, ITMS code 26230120002, funded by the European region development funds, ERDF). The maps were produced using the Generic Mapping Tools (Wessel and Smith, 1998) and the plots were prepared with the Python's Matplotlib module (Hunter, 2007).

## References

- Anderson E, Bai Z, Bischof C, Blackford S, Demmel J, Dongarra J, Du Croz J, Greenbaum A, Hammarling S, McKenney A, Sorensen D (1999) LAPACK Users' Guide, 3rd edn. Society for Industrial and Applied Mathematics, Philadelphia, PA, 520 pp
- Augustin M, Freeden W, Nutz H (2018) About the importance of the Runge–Walsh concept for gravitational field determination. In: Freeden W, Nashed MZ (eds) Handbook of Mathematical Geodesy: Functional Analytic and Potential Theoretic Methods, Birkhäuser, Cham, pp 517–560
- Balmino G (1994) Gravitational potential harmonics from the shape of an homogeneous body. *Celestial Mechanics and Dynamical Astronomy* 60:331–364
- Balmino G, Vales N, Bonvalot S, Briais A (2012) Spherical harmonic modelling to ultra-high degree of Bouguer and isostatic anomalies. *Journal of Geodesy* 86:499–520, doi: 10.1007/s00190-011-0533-4
- Barnouin OS, Daly MG, Palmer EE, Gaskell RW, Weirich JR, Johnson CL, Al Asad MM, Roberts JH, Perry ME, Susorney HCM, Daly RT, Bierhaus EB, Seabrook JA, Espiritu RC, Nair AH, Nguyen L, Neumann GA, Ernst CM, Boynton WV, Nolan MC, Adam CD, Moreau MC, Rizk B, Drouet DAubigny CY, Jawin ER, Walsh KJ, Michel P, Schwartz SR, Ballouz RL, Mazarico EM, Scheeres DJ, McMahon JW, Bottke WF, Sugita S, Hirata N, Watanabe SI, Burke KN, DellaGiustina DN, Bennett CA, Lauretta DS, The OSIRIS-REx Team (2019) Shape of (101955) Benu indicative of a rubble pile with internal stiffness. *Nature Geoscience* 12:247–252, doi: 10.1038/s41561-019-0330-x
- Barthelmes F (2013) Definition of functionals of the geopotential and their calculation from spherical harmonic models: Theory and formulas used by the calculation service of the International Centre for Global Earth models (ICGEM), <http://icgem.gfz-potsdam.de>. Scientific Technical Report STR09/02, GFZ German Research Centre for Geosciences, Potsdam, Germany, 32 pp
- Bucha B, Hirt C, Kuhn M (2019a) Cap integration in spectral gravity forward modelling: near- and far-zone gravity effects via Molodensky's truncation coefficients. *Journal of Geodesy* 93:65–83, doi: 10.1007/s00190-018-1139-x
- Bucha B, Hirt C, Kuhn M (2019b) Cap integration in spectral gravity forward modelling up to the full gravity tensor. *Journal of Geodesy* 93:1707–1737, doi: 10.1007/s00190-019-01277-3
- Bucha B, Hirt C, Kuhn M (2019c) Divergence-free spherical harmonic gravity field modelling based on the Runge–Krupar theorem: a case study for the Moon. *Journal of Geodesy* 93:489–513, doi: 10.1007/s00190-018-1177-4
- Chesley SR, Farnocchia D, Nolan MC, Vokrouhlický D, Chodas PW, Milani A, Spoto F, Rozitis B, Benner LAM, Bottke WF, Busch MW, Emery JP, Howell ES, Lauretta DS, Margot JL, Taylor PA (2014) Orbit and bulk density of the OSIRIS-REx target Asteroid (101955) Benu. *Icarus* 235:5–22, doi: 10.1016/j.icarus.2014.02.020
- Colombo OL (1981) Numerical methods for harmonic analysis on the sphere. Report No. 310, Department of Geodetic Science and Surveying, The Ohio State University, Columbus, Ohio, 140 pp
- Featherstone WE, Hirt C, Kuhn M (2013) Band-limited Bouguer gravity identifies new basins on the Moon. *Journal of Geophysical Research: Planets* 118:1397–1413, doi: 10.1002/jgre.20101
- Fecher T, Pail R, Gruber T (2015) Global gravity field modeling based on GOCE and complementary gravity data. *International Journal of Applied Earth Observation and Geoinformation* 35:120–127, doi: 10.1016/j.jag.2013.10.005
- Fecher T, Pail R, Gruber T, Schuh WD, Kusche J, Brockmann JM, Loth I, Müller S, Eicker A, Schall J, Mayer-Gürr T, Kvas A, Klinger B, Rieser D, Zehentner N, Baur O, Höck E, Krauss S, Jäggi A, Meyer U, Prange L, Maier A (2017) GOCO05c: A new combined gravity field model based on full normal equations and regionally varying weighting. *Surveys in Geophysics* 38:571–590,

- doi: 10.1007/s10712-016-9406-y
- Forsberg R, Tscherning CC (1981) The use of height data in gravity field approximation by collocation. *Journal of Geophysical Research* 86:7843–7854
- Förste C, Bruinsma SL, Abrikosov O, Lemoine JM, Schaller T, Götze HJ, Ebbing J, Marty JC, Flechtner F, Balmino G, Biancale R (2014) EIGEN-6C4 The latest combined global gravity field model including GOCE data up to degree and order 2190 of GFZ Potsdam and GRGS Toulouse. In: 5th GOCE User Workshop, Paris, France, 25–28 November
- Freeden W (1980) On the approximation of external gravitational potential with closed systems of (trial) functions. *Bulletin Géodésique* 54:1–20
- Freeden W, Schreiner M (2009) *Spherical Functions of Mathematical Geosciences: A Scalar, Vectorial, and Tensorial Setup*. Springer-Verlag, Berlin Heidelberg, 602 pp
- Fukushima T (2012) Numerical computation of spherical harmonics of arbitrary degree and order by extending exponent of floating point numbers. *Journal of Geodesy* 86:271–285, doi: 10.1007/s00190-011-0519-2
- Fukushima T (2017) Precise and fast computation of the gravitational field of a general finite body and its application to the gravitational study of asteroid Eros. *The Astronomical Journal* 154(145):15pp, doi: 10.3847/1538-3881/aa88b8
- Górski KM, Bills BG, Konopliv AS (2018) A high resolution Mars surface gravity grid. *Planetary and Space Science* 160:84–106, doi: 10.1016/j.pss.2018.03.015
- Gradshteyn IS, Ryzhik IM (2007) *Table of Integrals, Series, and Products*, seventh edn. Academic Press, 1172 pp
- Grafarend EW, Engels J (1993) The gravitational field of topographic-isostatic masses and the hypothesis of mass condensation. *Surveys in Geophysics* 140:495–524
- Grombein T, Seitz K, Heck B (2017) On high-frequency topography-implied gravity signals for a height system unification using GOCE-based global geopotential models. *Surveys in Geophysics* 38:443–477, doi: 10.1007/s10712-016-9400-4
- Gruber C, Novák P, Sebera J (2011) FFT-based high-performance spherical harmonic transformation. *Studia Geophysica et Geodaetica* 55:489–500, doi: 10.1007/s11200-011-0029-y
- Heiskanen WA, Moritz H (1967) *Physical Geodesy*. W. H. Freeman and Company, San Francisco, 364 pp
- Hirt C (2012) Efficient and accurate high-degree spherical harmonic synthesis of gravity field functionals at the Earth's surface using the gradient approach. *Journal of Geodesy* 86:729–744, doi: 10.1007/s00190-012-0550-y
- Hirt C, Kuhn M (2014) Band-limited topographic mass distribution generates full-spectrum gravity field: Gravity forward modeling in the spectral and spatial domains revisited. *Journal of Geophysical Research: Solid Earth* 119:3646–3661, doi: 10.1002/2013JB010900
- Hirt C, Kuhn M (2017) Convergence and divergence in spherical harmonic series of the gravitational field generated by high-resolution planetary topography—A case study for the Moon. *Journal of Geophysical Research: Planets* 122:1727–1746, doi: 10.1002/2017JE005298
- Hirt C, Reußner E, Rexer M, Kuhn M (2016) Topographic gravity modeling for global Bouguer maps to degree 2160: Validation of spectral and spatial domain forward modeling techniques at the 10 microgal level. *Journal of Geophysical Research: Solid Earth* 121:6846–6862, doi: 10.1002/2016JB013249
- Hirt C, Yang M, Kuhn M, Bucha B, Kurzmann A, Pail R (2019) SRTM2gravity: an ultrahigh resolution global model of gravimetric terrain corrections. *Geophysical Research Letters* 46:4618–4627, doi: 10.1029/2019GL082521
- Hobson EW (1931) *The Theory of Spherical and Ellipsoidal Harmonics*. Cambridge University Press, Cambridge, Great Britain, 500 pp
- Hotine M (1969) *Mathematical Geodesy*. U.S. Department of Commerce, Washington, D.C., 416 pp
- Hu X, Jekeli C (2015) A numerical comparison of spherical, spheroidal and ellipsoidal harmonic gravitational field models for small non-spherical bodies: examples for the Martian moons. *Journal of Geodesy* 89:159–177, doi: 10.1007/s00190-014-0769-x
- Hunter JD (2007) *Matplotlib: A 2D graphics environment*. *Computing in Science & Engineering* 9:90–95, 10.1109/MCSE.2007.55
- Jekeli C (1983) A numerical study of the divergence of spherical harmonic series of the gravity and height anomalies at the Earth's surface. *Bulletin Géodésique* 57:10–28
- Jekeli C (2017) *Spectral Methods in Geodesy and Geophysics*. CRC Press, 415 pp
- Jekeli C, Lee JK, Kwon JH (2007) On the computation and approximation of ultra-high-degree spherical harmonic series. *Journal of Geodesy* 81:603–615, doi: 10.1007/s00190-006-0123-z
- Krarpup T (1969) A contribution to the mathematical foundation of physical geodesy. *Meddelelse No. 44*, Geodætisk Institut, København
- Martinec Z (1998) *Boundary-Value Problems for Gravimetric Determination of a Precise Geoid*. Springer-Verlag, Berlin, Heidelberg, 223 pp
- Martinec Z, Pěč K (1989) The Phobos gravitational field modeled on the basis of its topography. *Earth, Moon, and Planets* 45:219–235
- Moritz H (1980) *Advanced Physical Geodesy*. Herbert Wichmann Verlag, Karlsruhe, Germany, 500 pp
- Moritz H (2000) Geodetic reference system 1980. *Journal of Geodesy* 74:128–133, doi: 10.1007/s0019000050278

- Moritz H (2003) The strange behavior of asymptotic series in mathematics, celestial mechanics and physical geodesy. In: Grafarend EW, Krumm FW, Schwarze VS (eds) *Geodesy: The Challenge of the Third Millennium*, Springer-Verlag, Berlin, Heidelberg, pp 371–377
- Nolan MC, Magri C, Howell ES, Benner LAM, Giorgini JD, Hergenrother CW, Hudson RS, Lauretta DS, Margot JL, Ostro SJ, Scheeres DJ (2013) Asteroid (101955) Bennu shape model V1.0. EAR-A-I0037-5-BENNUSHAPE-V1.0. NASA Planetary Data System, <https://sbn.psi.edu/pds/resource/bennushape.html>
- Pail R, Fecher T, Barnes D, Factor JF, Holmes SA, Gruber T, Zingerle P (2018) Short note: the experimental geopotential model XGM2016. *Journal of Geodesy* 92:443–451, doi: 10.1007/s00190-017-1070-6
- Pavlis NK (1988) Modeling and estimation of a low degree geopotential model from terrestrial gravity data. Report No. 386, Department of Geodetic Science, The Ohio State University, Ohio, USA, 173 pp
- Pavlis NK, Holmes SA, Kenyon SC, Factor JK (2012) The development and evaluation of the Earth Gravitational Model 2008 (EGM2008). *Journal of Geophysical Research* 117(B04406):1–38, doi: 10.1029/2011JB008916
- Rexer M (2017) Spectral solutions to the topographic potential in the context of high-resolution global gravity field modelling. PhD thesis, Technische Universität München, München, Germany, 212 pp
- Rummel R, Rapp RH, Sünkel H, Tscherning CC (1988) Comparisons of global topographic/isostatic models to the Earth's observed gravity field. Report No. 388, Department of Geodetic Science and Surveying, The Ohio State University, Columbus, Ohio, 33 pp
- Sacerdote F, Sansò F (2010) Least squares, Galerkin and BVPs applied to the determination of global gravity field models. In: Mertikas SP (ed) *Gravity, Geoid and Earth Observation: Proceedings of the IAG Commission 2: Gravity Field, Chania, Crete, Greece, 23–27 June 2008*, Springer, vol 135, pp 511–517, ISBN 978-3-642-10633-0, e-ISSN 978-3-642-10634-7
- Sansò F (1982) A note on density problems and the Runge–Krarup's theorem. *Bollettino di Geodesia e Scienze Affini* 41, 4:441–446
- Sansò F (1993) Theory of geodetic B.V.P.s applied to the analysis of altimetric data. In: Rummel R, Sansò F (eds) *Satellite Altimetry in Geodesy and Oceanography*, Springer-Verlag, Berlin, Heidelberg, pp 318–371, doi: 10.1007/BFb0117924
- Sansò F, Sideris MG (2013) *Geoid Determination: Theory and Methods*. Springer, Berlin, Heidelberg, 734 pp
- Sansò F, Sideris MG (2017) *Geodetic Boundary Value Problem: the Equivalence between Molodensky's and Helmert's Solutions*. Springer, 81 pp
- Sansò F, Reguzzoni M, Barzaghi R (2019) *Geodetic Heights*. Springer, 141 pp
- Sebera J, Bezděk A, Pešek I, Henych T (2016) Spheroidal models of the exterior gravitational field of asteroids Bennu and Castalia. *Icarus* 272:70–79, doi: 10.1016/j.icarus.2016.02.038
- Sjöberg L (1977) On the errors of spherical harmonic developments of gravity at the surface of the Earth. Report No. 12, Department of Geodetic Science, The Ohio State University, Columbus, Ohio, 74 pp
- Sjöberg L, Bagherbandi M (2017) *Gravity Inversion and Integration: Theory and Application in Geodesy and Geophysics*. Springer, 383 pp
- Sjöberg LE (2005) A discussion on the approximations made in the practical implementation of the remove-compute-restore technique in regional geoid modelling. *Journal of Geodesy* 78:645–653, doi: 10.1007/s00190-004-0430-1
- Sjöberg LE (2015) The topographic bias in Stokes formula vs. the error of analytical continuation by an Earth Gravitational Model – are they the same? *Journal of Geodetic Science* 5:171–179, doi: 10.1515/jogs-2015-0017
- Sjöberg LE, Bagherbandi M (2011) A numerical study of the analytical downward continuation error in geoid computation by EGM08. *Journal of Geodetic Science* 1:2–8, doi: 10.2478/v10156-010-0001-8
- Sneeuw N (1994) Global spherical harmonic analysis by least-squares and numerical quadrature methods in historical perspective. *Geophysical Journal International* 118:707–716
- Šprlák M, Han SC, Featherstone WE (2018) Forward modelling of global gravity fields with 3D density structures and an application to the high-resolution ( $\sim 2$  km) gravity fields of the Moon. *Journal of Geodesy* 92:847–862, doi: 10.1007/s00190-017-1098-7
- Sun W, Sjöberg LE (2001) Convergence and optimal truncation of binomial expansions used in isostatic compensations and terrain corrections. *Journal of Geodesy* 74:627–636
- Virtanen P, Gommers R, Oliphant TE, Haberland M, Reddy T, Cournapeau D, Burovski E, Peterson P, Weckesser W, Bright J, van der Walt SJ, Brett M, Wilson J, Jarrod Millman K, Mayorov N, Nelson ARJ, Jones E, Kern R, Larson E, Carey C, Polat I, Feng Y, Moore EW, VanderPlas J, Laxalde D, Perktold J, Cimrman R, Henriksen I, Quintero EA, Harris CR, Archibald AM, Ribeiro AH, Pedregosa F, van Mulbregt P, SciPy 10 Contributors (2020) *SciPy 1.0: Fundamental Algorithms for Scientific Computing in Python*. *Nature Methods* 17:261–272, doi: 10.1038/s41592-019-0686-2
- Wang YM (1997) On the error of analytical downward continuation of the earth's external gravitational potential on and inside the earth's surface. *Journal of Geodesy* 71:70–

82

- Wang YM, Saleh J, Roman DR (2012) The US Gravitometric Geoid of 2009 (USGG2009): model development and evaluation. *Journal of Geodesy* 86:165–180, doi: 10.1007/s00190-011-0506-7
- Wessel P, Smith WHF (1998) New, improved version of generic mapping tools released. *EOS, Transactions American Geophysical Union* 79:579, doi: 10.1029/98EO00426
- Wieczorek MA (2015) Gravity and topography of the terrestrial planets. In: Schubert G (ed) *Treatise on Geophysics*, 2nd edn, Elsevier, chap 10.5, pp 153–193, doi: 10.1016/B978-0-444-53802-4.00169-X
- Wieczorek MA, Phillips RJ (1998) Potential anomalies on a sphere: Applications to the thickness of the lunar crust. *Journal of Geophysical Research* 103:1715–1724